Contra-directional couplers as optical filters on the silicon on insulator platform

Mémoire

Jonathan St-Yves

Maîtrise en génie électrique
Maître ès sciences (M.Sc.)

Québec, Canada

Contra-directional couplers as optical filters on the silicon on insulator platform

Mémoire

Jonathan St-Yves

Sous la direction de:

Sophie Larochelle, co-directrice de recherche
Wei Shi, directeur de recherche

Résumé

Ce mémoire vise à étudier la conception, la fabrication et la caractérisation de filtres à base de coupleurs contra-directionels en silicium. Ceux-ci sont un type de filtre optique encore peu connu, semblable à des réseaux de Bragg, mais réfléchissant dans un autre guide d'onde.

Afin de comprendre pourquoi les filtres optiques sont importants à améliorer, ce mémoire commence en expliquant la base des communications optiques. Sont ensuite expliqués les principes de la photonique sur silicium, et comment arriver à manipuler la lumière à l'aide des matériaux utilisés en électronique. Les différents dispositifs existants en silicium sont énumérés, avec une attention particuliére portée aux filtres optiques.

Le principe de fonctionnement des coupleurs contra-directionels est expliqué en détail au chapitre 2. Celui-ci reformule les principes de base connus, en rajoutant des détails sur la simulation de l'apodization et du bruit de phase.

La recherche originale en laboratoire à ce sujet est exposée dans les chapitres 3 et 4. Le premier article démontre qu'il est possible de fabriquer des coupleurs contra-directionels avec un processus de photolithographie malgré la précision requise. Le deuxième utilise des coupleurs contra-directionels pour créer un filtre accordable ayant la plus grande plage d'accordabilité mesurée sur silicium.

Tester ces dispositifs fut une part importante du travail et de l'apprentissage. Ainsi, le dernier chapitre est consacré à la caractérisation des dispositifs sur silicium à l'aide d'un montage automatisé. Ce chapitre a pour but d'expliquer en détail toutes les étapes du design, de l'alignement et des tests afin de documenter la procédure pour les nouveaux étudiants.

Au final, ce travail démontre que les coupleurs contra-directionels en silicium sont une solution envisageable pour plusieurs applications nécessitant des filtres optiques, tel que les réseaux reconfigurables et les canaux de communication large bande.

Abstract

This memoir aims to study the design, fabrication and characterization of filters based on contra-directional couplers on silicon. These are a type of filter still little known, similar to Bragg gratings, but reflecting the light in an other waveguide.

To understand why optical filters are important to improve, this memoir starts by introducing the basis of optical communications. The principles of silicon photonics are then explained, to understand how to manipulate light using micro-electronics materials. The devices available on silicon are enumerated, with a special attention given to optical filters.

Contra-directional couplers are explained in detail in chapter 2. This chapter explains the known principles, adapting them to be able to simulate apodization and phase noise in these devices.

The original laboratory research is shown in chapters 3 and 3. The first article demonstrates that it is possible to fabricate contra-directional couplers using photolithography despite the small features required. The second one uses contra-directional couplers to create a tunable filter displaying the greatest tunable bandwidth range measured in silicon filters.

Testing these devices has been an important part of the work. The last chapter is about the characterization of silicon devices using an automated setup. This chapter aims to explain all the details of the design, alignment and test to document the procedure for future students.

In sum, this work shows that silicon contra-directional couplers are an appealing solution for many applications which require optical filters such as reconfigurable networks and broadband channels.

I would like to thank

Marie-Chistine, for the love, kindness and support. You've been at my side along all of this. I love you my dear!

Bertrand and Marlene, for being the best parents.

Lydie and Jean-Yves for the soup, among all the innumerable little things.

Dobby, Daisy and Sunny, our canine companions, who always manage to cheer us up.

Raphael, William, Alexandre, Philippe and Antoine, for all the fun, the great discussions and keeping the office lively.

Philippe Chretien, for having solutions to every problem in the lab.

Brian Beggs, my elementary school English teacher, for giving me access to all the knowledge this language contains and keeping me challenged for three years.

All of my science teachers, who managed to transmit their passion and curiosity.

Sophie LaRochelle, for her great insight and expertise on all the details I've missed.

Wei Shi, for his guidance and being a great partner through this project. Wei has put as much into this research as me, he's been the source of many ideas and managed to keep me on the right path. I could not have wished for a more thoughtful and comprehensive mentor!

Thank you very much everyone for your direct or indirect contribution!

This project would not have been possible without the funding of NSERC, TeraXion, PROMPT and CMC Microsystems. Huge thanks to our partners!

Contents

List of Tables

List of Figures

List of Abbrevations

DC	Directional Coupler
CDC	Contra Directional Coupler
WDM	Wavelength Division Multiplexing
SOI	Silicon On Insulator
TE	Transverse Electrical
TE	Transverse Magnetic
GC	Grating Coupler
FGC	Fiber Grating Coupler
MMI	Multimode Interferometer
FDTD	Finite Difference Time Domain
MZI	Mach Zehnder Interferometer
e-beam	Electron Beam
DUV	Deep-ultraviolet
BW	Bandwidth
ISI	Inter-Symbol Interference
SLSR	Sidelobes Suppression Ratio
FSR	Free spectral range
CMOS	Complementary metal-oxide-semiconductor
SEM	Scanning electron microscope
MR	Micro-Ring
OVA	Optical Vector Analyzer
VNA	Vector Network Analyzer
BERT	Bit Error Rate Tester
PM	Polarization Maintaining
SSE	Spontaneous Source Emission
LED	Light Emitting Diode
RF	Radio Frequency

List of Variables

n	Material index
Δn	Material index difference, contrast
n_{eff}	Effective index of a mode
c	Speed of light (299 792 458 m/s)
f	Frequency
λ	Wavelength in vacuum
L	Length
L_c	Crossover distance (in a coupler)
w_x	Width of part x
T	Temperature
L_o	Optical length ($L * n_{\text{eff}}$
$\Delta\phi$	Phase difference
Λ	Period or pitch of a grating
z	Position along the z axis (usually defined as the propagation direction)
E	Electric field amplitude and phase
κ_{xy}	Coupling coefficient from mode x to y
β_x	Propagation constant of mode x
λ_D	Dropped central wavelength
C	Left-to-right transfer matrix
ω	Radial frequency ($2\pi f$)
ϵ	Dielectric constant of the material
x	Position along the x axis
y	Position along the y axis
a	Coefficient of the gaussian profile
g	Average gap between the waveguides in a coupler
N	Number of corrugations
lch	Amount of linear chirp
kch	Amount of coupling dependent chirp
rch	Amount of random chirp
θ	Angle

Chapter 1

Silicon Photonics — Overview and principles

1.1 Introduction and motivation

The Internet is a revolution of an importance that cannot be overstated. It allows humans all over the world to communicate more than ever before. It allows anyone connected to the network to access most of the knowledge of mankind within seconds. It creates new industries, and new paradigms for existing ones.

And after all these years of improvement, demand for high speed communication is still increasing. Much like broadcast television, and broadcast radio before it, on demand video is becoming a cultural point of reference for many, allowing users to easily access the best content which is relevant to their interest. Big databases for services such as Facebook and Google need to constantly answer complex queries from millions of users. Users want all of their personal data to be accessible in their device in all locations. All of these applications would benefit from more capacity of data transfer.

This infrastructure consumes large amounts of energy, meaning that improvements in energy efficiency, speed and cost have a large impact. Optical communications using silicon photonics offer promising solutions. Communicating by moving photons takes less energy than using electrons, and the compactness of silicon photonics promises very high speed operation at low cost.

1.2 Optical communications

In order to appreciate the challenges of optical communication devices, one must understand the basic principles of optical communication systems.

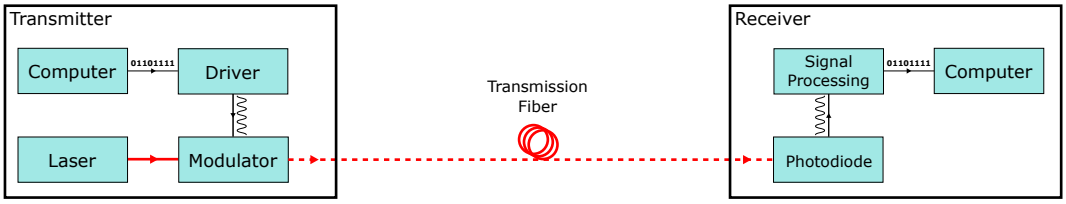

Figure 1.1: Schematic of a simple optical communication system

Figure 1.1 shows the schematic of a simple optical communication system with all the required components. At the transmitter, the data we want to deliver from a computer is sent to the modulator driver, which is an electrical component responsible for creating a high frequency signal with the right voltage. This voltage is applied to the input of an electro-optical modulator, which modulates the output of a continuous wave laser, often by simply quickly flickering the light on or off. This modulated optical signal is then transferred through an optical fiber. At the receiver, the light is absorbed by a photodiode, which makes charges mobile from the interaction with photons. Collecting these charges creates a signal similar to the one produced by the driver, which is then analyzed using electrical signal processing to recreate the original digital data.

The point of using optical communication instead of regular electrical communications is twofold. First, optical fibers have much lower attenuation over distance then electrical cables, typically lower than 1 dB/km compared to tens of dB/km. This is critical when communicating over large distances. Second, optical fibers have a bandwidth several orders of magnitudes larger then even the most fancy electrical cables with expensive shielding. This allows low cost fibers to carry much more data at once. Other important advantages include the small dimensions and weight of optical fibers, their better durability and isolation from environmental noise.

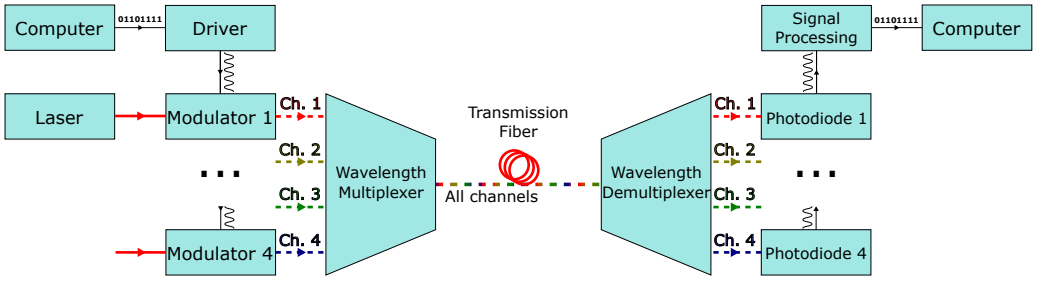

Figure 1.2: Schematic of a communication system with Wavelength Division Multiplexing

Since the modulators are driven by electrical signals, each channel can at best only achieve a bandwidth in the 10 gigahertz (GHz, 10^9 Hz) order of magnitude with on-off modulation, while the optical bandwidth of a fiber is of several terahertz (THz, 10^{12} Hz). It is possible to combine multiple signals into the same fiber, as seen in figure 1.2 using the technique

know as wavelength division multiplexing (WDM) which is analogous to frequency division multiplexing, used in systems such as radio broadcast. This way, the fiber can in theory be used to its full potential when thousands of electrical inputs are multiplexed in the same physical fiber. Other multiplexing techniques such as mode division multiplexing and polarization multiplexing can be used simultaneously with WDM, but these usually require special fibers and/or coherent receivers with digital signal processing.

1.3 Fabrication techniques

In order to understand the possibilities and constraints of the SOI platform, is it useful to study the fabrication technique itself. Silicon is usually patterned following a lithographic procedure that can be broadly described as follows:

1. Apply a photoresist on top of a full silicon wafer, a large disk. This is often done with a process called spin-coating.
2. Make the photoresist hard or soft in a pattern following the design, by directing photons or electrons at the surface. This is called the exposition.
3. Remove the soft photoresist using selective chemicals. This is the development.
4. Etch the uncovered silicon with chemicals such as ions. Only the silicon covered with hard photoresist remains, creating the waveguides.

The processes use different ways to pattern the photoresist. They vary in cost, flexibility, fabrication delay and resolution.

1.3.1 Electron beam lithography

Electron beam lithography (commonly referred to as e-beam) uses a beam of electrons to selectively harden the photoresist. The beam must be swept across all the areas were silicon is kept. This is a time-consuming process, but large areas without silicon do not take additional time.

Since there are few steps and this kind of equipment is available in many facilities, the prototype can be delivered within a month. The resolution of minimal feature sizes are very small, often under 50 nanometers.

1.3.2 Deep-ultraviolet lithography

More suitable to mass production, the optical lithography process starts by creating a "mask" with e-beam. To harden the photoresist, light (usually in the deep-ultraviolet spectrum) is

shined through the mask in a single exposition. It is thus possible to repeat the pattern at a low cost once the mask is fabricated.

The mask must have a filling density within a certain range, often requiring all unused areas to be covered in tiled with that density. A single chip is thus more expensive than with e-beam since the mask fabrication takes longer and the additional steps require specialized facilities. The minimal feature size is also larger, usually over 100 nm, due to the much larger wavelength and diffraction effects of ultra-violet light compared to electrons.

These facilities however offer more options as part of a standard process such as dopants, metals and multi-level etch. Since high-volume low-cost commercial products use this technique, prototypes targeting this market often use it and the lithography limits must be kept in mind.

1.4 Silicon on insulator optical devices

Historically, the multiple devices needed in optical communications were all in separate packages and assembled into a system. The goal of integrated optics is to reduce the size and cost of these devices, and integrate them in a single component.

The proposed architecture consists of a silicon on insulator (SOI) chip, which can both be used for electronics and for photonics operations. SOI is an industry standard to fabricate electronic devices, therefore the fabrication technology is already advanced and available. For optics, both silicon and silicon oxide (glass, the insulator) are transparent in the near infrared spectrum. This section explains how to use the physical properties of these materials to manipulate light.

1.4.1 Optical waveguides

Waveguides are a fundamental building block of optics. They allow us to connect devices to each other on the chip and are also often a critical part of the device itself.

The most standard optical waveguide is a glass fiber, which can be bent in any direction and carry the light to over kilometers with minimal optical losses. It does so by doping the core with germanium, slightly increasing the refractive index in the center. This index contrast allow the light to be guided in a manner analogous to total internal reflection along the core of the fiber.

While optical fibers have a cylindrical symmetry, it is also possible to guide light with a rectangular waveguide. Figure 1.3 shows how such a waveguide, typically used in silicon photonics, compares to a typical telecommunication fiber. While the index contrast Δn between germanium-doped oxide (green) and silicon oxide (blue) is only of about 1%, the index n of silicon is of 3.4 versus 1.4 for silicon oxide. This much larger contrast allows single mode

waveguides to be smaller, at a size of about 210 by 500 nanometers (nm) for the silicon waveguide, against about 8 microns (µm) for a fiber. The vertical dimension is constrained by the fabrication process, while the horizontal dimension is chosen to be small enough to only guide the fundamental modes (more on this later).

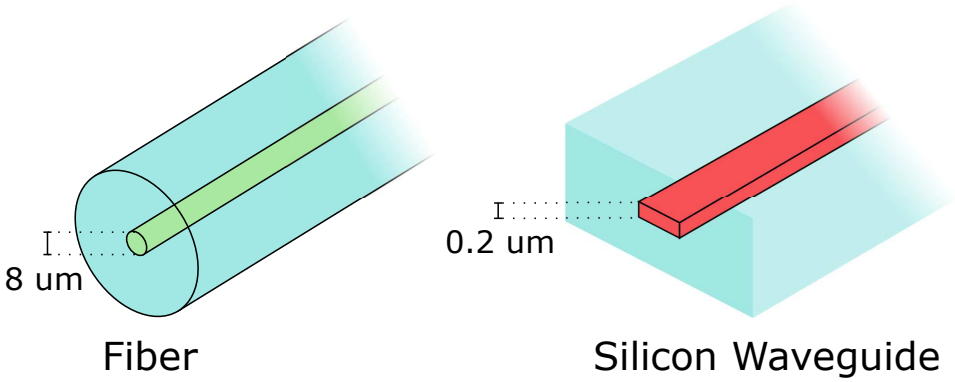

Figure 1.3: Single mode optical fiber compared to a single mode silicon waveguide

These waveguides typically cause loss of about 1 decibel per centimeter (dB/cm) due to material absorption and scattering loss caused by waveguide non-uniformity, also called sidewall roughness. Since the length of silicon photonics devices are usually under a millimeter (mm), this relatively high loss is acceptable. Due to the large index contrast and high confinement, waveguide bends can have a radius as small as 5 µm.

An useful property of waveguides is the effective index n_{eff}. Falling somewhere between the refractive index of both materials, the effective index tells us the phase velocity $v = c/n_{\text{eff}}$ where c is the speed of light, as well as the wavelength in the medium $\lambda_n = \lambda/n_{\text{eff}}$, where λ is the wavelength in vacuum $\lambda = c/f$, with f being the optical frequency. This effective index can be approximated using the analytical effective index method and be calculated with more precision using a numerical mode solver such as Lumerical MODE. Single-mode waveguides only guide the fundamental transverse electrical (TE) and transverse magnetic (TM) modes (see Fig. 1.4), while larger waveguides can also guide higher order modes. Each mode has a different effective index. Devices that do not require multiple modes often only use the TE mode since it is the one with the highest confinement, allowing for a smaller bend radius.

1.4.2 Optical inputs and outputs

If we want two chips that are not directly adjacent to communicate with each other, the light needs to be carried by an optical fiber at some point. Thus, the small silicon waveguides need

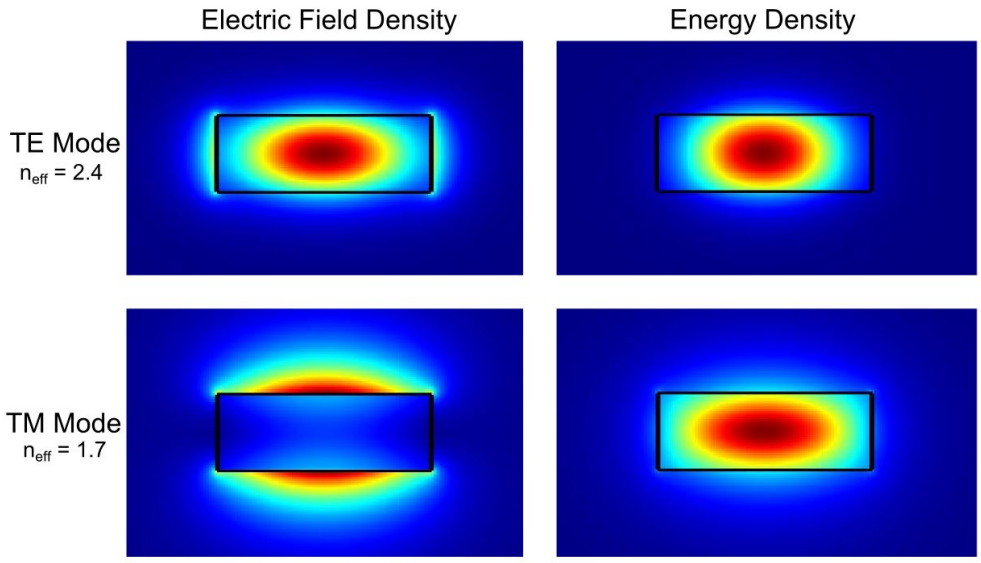

Figure 1.4: Comparison of the TE and TM mode in a 500 by 210 nm waveguide at $\lambda = 1550$ nm. The structure is delimited by a black line.

to interface with the large fibers, which is not trivial considering the large index difference and mode mismatch. Two methods are popular: edge coupling and fiber grating couplers.

Edge-coupling

The most straightforward way of coupling light from a chip to a fiber and vice-versa is to physically put them in front of each other. However, doing this with a regular waveguide would have a very low optical transmission since the modes are very mismatched. By narrowing the silicon waveguide horizontally, a larger mode size can be achieved, resulting in good transmission efficiency (loss of under 1 dB).[2] The transition from a regular waveguide to a mode-matching waveguide is done gradually with an adiabatic taper. Since the waveguides can only be in the plane of the silicon layer, such couplers need to be on the edge of the chip.

Fiber grating coupler

Another common technique is to use a fiber grating coupler [42] (FGC or GC) which is a grating that diffracts the light from near-vertical incidence to the plane of the chip. Compared to edge couplers, these can be placed anywhere on the surface of the chip, but they may have higher insertion loss (typically 5-7 dB) and cover a smaller bandwidth.

These are advantageous when prototyping many devices with multiple inputs and outputs, but the insertion loss is usually too high for the power budget available in commercial applications. Due to the better placement flexibility and available equipment, all of the measurements used in this memoir were made with FGCs.

Figure 1.5 shows two types of such grating couplers. Linear grating couplers are the more primitive version showcasing the principle. It is generally preferable to use focusing fiber grating couplers which guide the light into the waveguide in a more compact and efficient way.

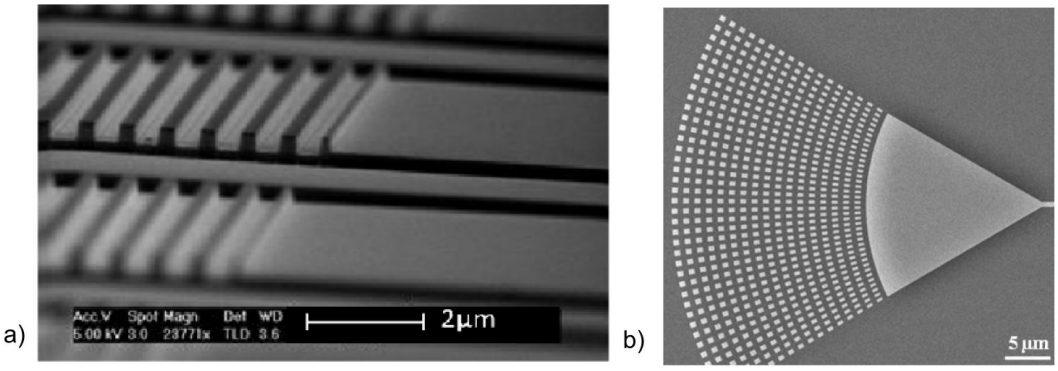

Figure 1.5: a) Linear fiber grating couplers. b) Focusing fiber grating couplers. Figures from [35, 42]

1.4.3 Lasers

Lasers can potentially be integrated to the platform by selectively growing a gain medium unto the chip, such as semi-conductor compounds. The process is usually called hybrid III-V integration where III-V refers to the third and fifth column of the periodic table. This gain medium can be coupled to the other silicon chip devices, which can provide the resonating cavity needed for laser operation.

1.4.4 Photodiodes

Germanium can be epitaxially grown on top of silicon. Since germanium has an higher refractive index and is not transparent in the near infrared, light propagating in the silicon waveguide will be coupled into it and be absorbed, generating electron and hole pairs. By connecting conductors such as doped silicon or metal to the germanium, these charges can be collected and form a current output, effectively transforming an optical signal to an electrical one.

1.4.5 Splitters

Optical splitters have a variety of applications and are often building blocks for more complicated devices such as resonators.

Directional coupler

A simple way to couple a part of the light in a waveguide to another one is to put identical waveguides close to each other. The wave will be guided by both waveguides, bouncing from

one to the other over a cross-over distance L_c. The closer the waveguides, the shorter L_c. By only putting the waveguides close to each other for a fraction of this length, it is possible to partially couple the light for any ratio. L_c is a function of wavelength since shorter wavelengths are more confined, causing less coupling, but it is possible to have a wide bandwidth with the same coupling ratio by using more complex waveguides if necessary. [39]

Multimode interferometer

By connecting single-mode waveguides to one side of large multimode waveguide, one can excite many modes. After propagating over a distance, these modes will interfere with each other and create an interference pattern, which can be collected by waveguides on the other side. These interferometers have the advantage of having any number of ports on both sides and being very customizable with arbitrary power splitting, but the response is often quite sensitive to wavelength as well as fabrication variance. [36]

Y-branch

A special case of multimode interferometer is the Y-branch, a symmetrical design which aims to split a single beam in two equal parts, with minimal losses and over a wide bandwidth. By having only one input in the center, there is no preferential direction, ensuring a 50/50 split. The shape was optimized with simulation software to produce the one shown in figure 1.6 [41].

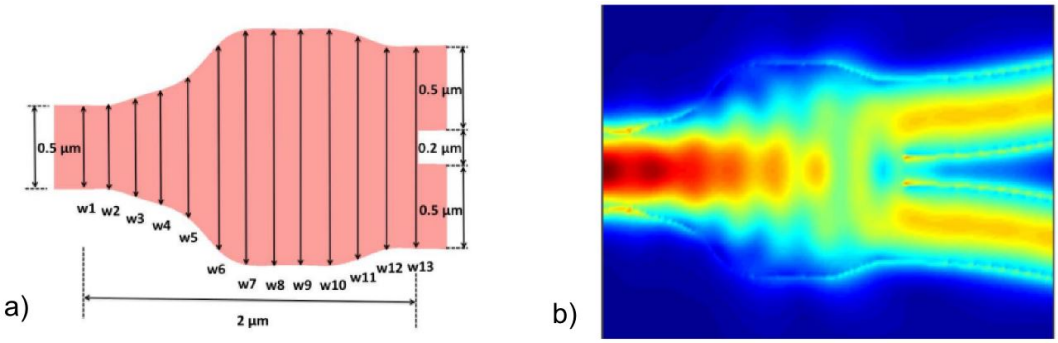

Figure 1.6: a) Y-branch schematic showing the various widths optimized. b) A simulation result of the electric field propagation in FDTD. Figures from [41]

1.4.6 Modulators

Amplitude modulators need to shutter a continuous laser on or off, acting as very fast switches. The faster the switch, the faster information can be encoded into the light. Multiples devices can be used to achieve this.

Mach Zehnder interferometer

A common way to extinguish the laser is to create destructive interference. The laser beam is divided, then recombined with one beam having a π phase shift compared to the other.

This system , shown in figure 1.7a usually uses a y-branch on both sides to divide and combine the beam, with an electrical phase shifter on each propagation arm between them [9]. There are two common ways to change the phase.

1. Thermal phase shifter: Silicon refractive index has a temperature dependence of $\mathrm{d}n_{\mathrm{Si}}/\mathrm{d}T = 1.87{\times}10^{-4}\mathrm{K}^{-1}$ at room temperature for wavelengths around 1550 nm [7]. Using micro-heaters, we can locally change the refractive index in one arm, causing the optical length $L_o = L * n_{\mathrm{eff}}$ to change slightly, which changes the phase at the end. By increasing L_o by $\lambda/2$, one can obtain a π phase shift and destructive interference.
2. Plasma dispersion effect: Since electrical carriers interact with light, changing the carrier distribution in the waveguide changes the refractive index. By creating a P-N junction over the silicon waveguide, carriers are present where light travels. Applying a positive voltage over such a junction injects carriers [34], while applying a negative voltage varies the depletion region in a reverse biased junction [16].

All of these effects have a limited speed of operation, in order from the slowest to the fastest being thermal, carrier injection and carrier depletion. Since carrier depletion is the fastest, it is the one most often used to shift the phase in high-speed modulators.

Micro-ring modulator

The principle behind micro-ring resonator is that light is coupled into a circular cavity. When the optical length of this cavity is a multiple of the wavelength, resonance occurs, causing a high concentration of energy in the ring which is dissipated, essentially cutting off this wavelength in the transmission.[15] [6]

To use this principle in modulators, a phase shifter in the ring cavity allows us to change the optical length of the cavity, as shown in figure 1.7b Changing the optical length of the cavity can cause a given wavelength to switch from resonance to no resonance.

1.4.7 Filters

Filters are optical structures which have wavelength dependent behavior. These have two main purposes in optical communication systems

1. Separating channels in WDM as a demultiplexer. The input from a single waveguide is divided into two or more waveguides, similarly to splitters, but in a wavelength dependent

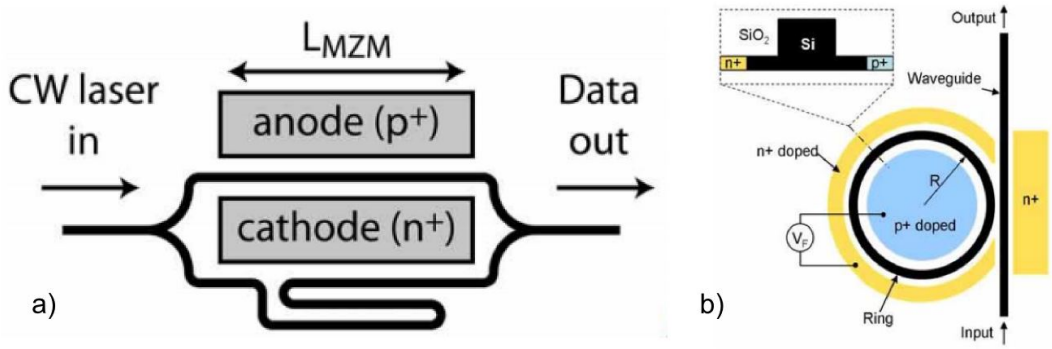

Figure 1.7: a) Mach Zehnder interferometer modulator . b) Ring modulator. Figures from [9, 37]

way. Since optical devices are reciprocal, using this the other way around allows us to combine multiple channels together for a multiplexer.

2. Separating signal from out-of-band noise. When a single signal of interest is present along with noise (from neighboring channels or from amplifiers), the quality of the reception can be increased by filtering out out-of-band noise.

Lattice filters

Lattice filters use the previously mentioned Mach Zehnder interferometer structure, but instead of creating the π phase shift with electrodes, there is a constant delay of length ΔL in one arm compared to other. This causes a phase shift proportional to the frequency $\Delta\phi = 2\pi\frac{n_{\text{eff}}L}{c}f$, which means that for each increase of the phase $\Delta\phi$ by 2π there will be a succession of destructive and constructive interference.

This creates a filter with periodic pass-band and stop-band. By cascading a few of these with different delays and power splitting, it is possible to divide the signal in multiple channels with a custom shape depending on the application [11]. These filters are however very sensitive to the variations of n_{eff} caused by chromatic dispersion and fabrication variance.

Arrayed waveguide gratings and Echelle gratings

These filters use multiple interfering beams with slightly different phase to again create periodic channels. Arrayed waveguide gratings splits the power into multiple waveguides, each a bit longer then the previous one, and then makes them interfere in an MMI-like region.

Echelle gratings are similar, but the splitting and interference happen in the same region, with the phase shift caused by a series of reflection facets at increasing distance of the back side of this region. [17]

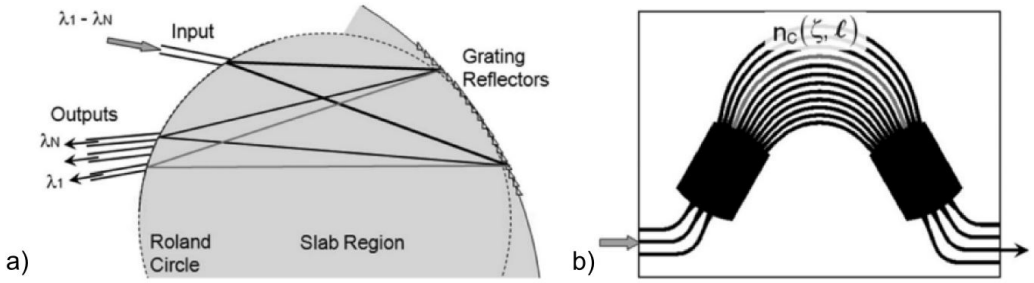

Figure 1.8: a) Echelle Grating. b) Arrayed waveguide grating. Figures from [17]

Bragg-grating

Bragg gratings act like mirrors, but only for a portion of the spectrum. They are reflective filters where most of the light goes through. Using a periodic perturbation of the effective index with a period Λ, a part of the spectrum around $\lambda = 2n_{\text{eff}}\Lambda$ is reflected. This equation is referred as the Bragg condition. When the condition is met, all of the wavefronts reflected at each index change are in phase, creating a backward propagating wave.

This device is well known and commonly used in fiber [14]. However, the goal is rarely to send the light back were it came from. Many applications (such as multiplexers) require a circulator, which is able to separate the forward and backward propagating beams. However, these circulators are made out of magnetic materials [31] which are incompatible with standard silicon photonics process, making Bragg gratings limited in their applications on this platform. Recently, operation without a circulator has been demonstrated using an interferometer design.[28]

Contra-directional couplers

Contra-directional couplers (also known as CDC or contra-DC) share many properties with Bragg gratings, but unlike the latter, the dielectric perturbation creates a backward propagating wave in another waveguide at close proximity. This solves the problem caused by the absence of circulators since the input and filtered output are no longer in the same waveguide.

However, contra-directional couplers must be modeled differently, and have particular challenges that must be addressed. They are the main topic of this memoir and are presented in detail in chapter 2.

1.5 Conclusion

This enumeration of devices available on the silicon platform aims to show that all of the functions needed to achieve optical data transmission are possible within this single process.

Integration has been a key aspect of the ever decreasing cost of electronics, and same thing can now happen to optical communications.

More research keeps on pushing the boundary of what is possible in this promising new platform, and this memoir aims to understand and improve upon what could be a key component of future products.

Chapter 2

Contra-directional couplers — Principles and simulation

This chapter describes the fundamental and operating principles of contra-directional couplers, based on [21]. It covers the physical structure, as well as the phenomena observed in this structure and how to simulate them. Beyond re-interpreting this article, this chapter also describes the methodology to simulate apodized contra-directional coupler response and provide an analysis of the phase noise present in fabrication.

2.1 Principle of operation

Contra-directional couplers (contra-DCs or CDCs) are similar to directional couplers in geometry — two waveguides that are placed very close to each other, allowing coupling between them. Compared to directional couplers, there are two main differences. First, the waveguides do not have the same width. This lead to different propagation constants in the waveguides and suppresses the normal co-directional coupling. Second, a periodic dielectric perturbation causes light at a certain wavelength to be coupled into the other waveguide in the backward direction, similar to how Bragg gratings operate.

2.2 Geometry

Figure 2.1 shows a schematic of a contra-DC, with the tapers needed to readily connect to routing waveguides. Both the width and the spacing between the waveguides must be adiabatically changed with tapers to interface between the grating section and the routing waveguides.

The grating section is where light is reflected. Figure 2.2 shows a close up on this structure. In this research, the waveguides are made of silicon, covered on all sides by silicon dioxide. The

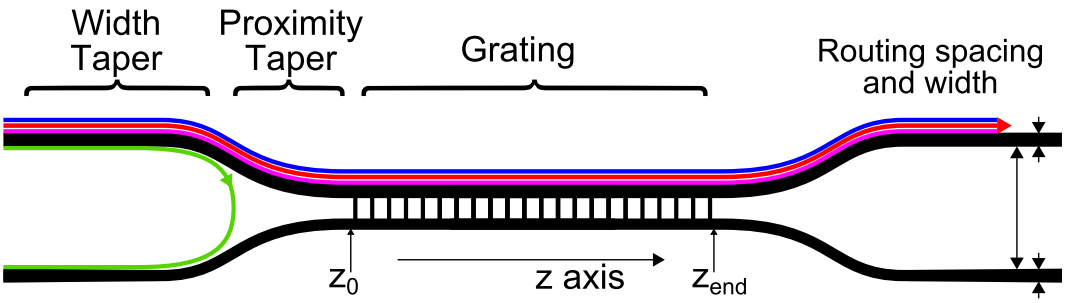

Figure 2.1: Components of a contra-directional coupler, with connections to routing waveguides. Colors show how different frequencies are either reflected or go through.

top and bottom waveguides have different widths w_1 and w_2, resulting in different effective indices of the mode mainly confined in each ($n_{\text{eff},1}$ and $n_{\text{eff},2}$). A perturbation of constant period Λ is etched on both the inside and outside walls of each waveguide, creating alternating sections of smaller and large waveguides gap. The outside wall is patterned in this way to keep the effective index the same in both the close and far sections in order to reduce the Bragg reflections in the input waveguide [23].

In this configuration, only the band around wavelength λ_D is coupled from the input to the drop port, while the rest of the light goes through. The second-order coupling would be at $\lambda_D/2$ where silicon is not transparent, assuming λ_D is in the telecommunication band from around 1200 to 1600 nm.

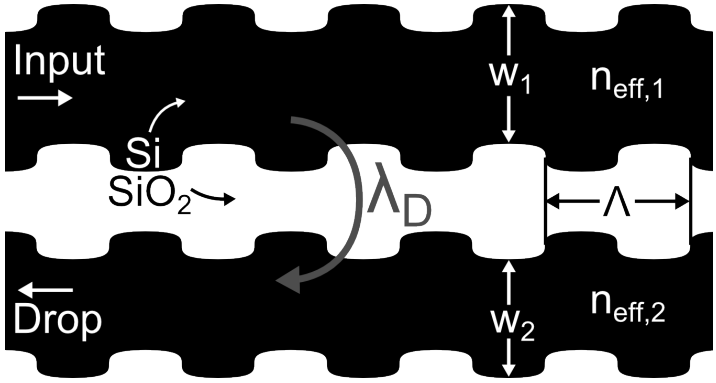

Figure 2.2: Schematic of the grating section with sidewall corrugations.

2.3 Formalism

The steady state electric intensity and phase for each cross-section along the propagation direction z is $E(z)$,

$$E(z) = \begin{bmatrix} A^+(z) \\ B^-(z) \\ A^+(z) \\ B^-(z) \end{bmatrix} \tag{2.1}$$

where A is the component mainly confined in the top waveguide (first super-mode), B in the bottom one (second super-mode); and + and - denote the forward and backwards propagating fields respectively.

Thus, the goal in a regular drop filter would be to transfer the energy from $A^+(z_0)$ to $B^-(z_0)$ around a specific wavelength, with the rest of the energy going to $A^+(z_{\text{end}})$.

In a symmetrical add-drop filter, the energy from $B^-(z_{\text{end}})$ would also be sent to $A^+(z_{\text{end}})$ for the same wavelength. This symmetry naturally occurs in contra-DC since the coupling from waveguide A to B κ_{12} is equal to the coupling from B to A κ_{21}.

In order to transfer the energy this way, a periodic dielectric perturbation is used along the propagation axis. Sidewalls corrugations are often used to produce this perturbation since the fabrication process is often limited to 2 dimensional geometry when high accuracy and uniformity are required.

The period of this perturbation Λ must be

$$\Lambda = \frac{2\pi}{\beta_1 + \beta_2} \tag{2.2}$$

or in terms of λ_D

$$\Lambda = \frac{\lambda_D}{n_{\text{eff},1} + n_{\text{eff},2}} \tag{2.3}$$

with $\beta = \frac{2\pi n_{\text{eff}}}{\lambda_D}$.

2.4 Coupled mode matrices

The transfer matrix method is used to calculate the filter response for each λ. By calculating C, the total left-to-right transfer matrix, we can find the relationship between $E(z_0)$ and $E(z_{\text{end}})$.

$$E(z_0) = C(z_0, z_{\text{end}})E(z_{\text{end}}) \tag{2.4}$$

For the general case of an apodized coupler (see section 2.6), the C matrix can be calculated with the product of multiple segments along the propagation direction.

$$C(z_0, z_{\text{end}}) = \prod_{i=1}^{n} C(z_{i-1}, z_i) = \prod_{i=1}^{n} e^{(z_i - z_{i-1})S_{1,i}} e^{(z_i - z_{i-1})S_{2,i}} \tag{2.5}$$

where the matrix exponentials can be calculated using the function *expm()* implemented in Matlab [1]. The matrices S_1 and S_2 change for each subsection i and are given by

$$S_1 = \begin{bmatrix} j\Delta\hat{\beta}_1 & 0 & 0 & 0 \\ 0 & j\Delta\hat{\beta}_2 & 0 & 0 \\ 0 & 0 & -j\Delta\hat{\beta}_1 & 0 \\ 0 & 0 & 0 & -j\Delta\hat{\beta}_2 \end{bmatrix} \tag{2.6}$$

and, assuming constant length section is used such that $z_i - z_{i-1} = z_c$,

$$S_2 = \begin{bmatrix} -j\Delta\hat{\beta}_1 & 0 & -j\kappa_{11}e^{j2\Delta\hat{\beta}_1 z_c} & -j\kappa_{12}e^{j(\Delta\hat{\beta}_1+\Delta\hat{\beta}_2)z_c} \\ 0 & -j\Delta\hat{\beta}_2 & -j\kappa_{12}e^{j(\Delta\hat{\beta}_1+\Delta\hat{\beta}_2)z_c} & -j\kappa_{22}e^{j2\Delta\hat{\beta}_2 z_c} \\ j\kappa_{11}^* e^{-j2\Delta\hat{\beta}_1 z_c} & j\kappa_{12}^* e^{-j(\Delta\hat{\beta}_1+\Delta\hat{\beta}_2)z_c} & j\Delta\hat{\beta}_1 & 0 \\ j\kappa_{12}^* e^{-j(\Delta\hat{\beta}_1+\Delta\hat{\beta}_2)z_c} & j\kappa_{22}^* e^{-j2\Delta\hat{\beta}_2 z_c 1} & 0 & j\Delta\hat{\beta}_2 \end{bmatrix} \tag{2.7}$$

where the $\Delta\hat{\beta}$ and κ are calculated individually for each of the n sections and considered constant within these, with $\Delta\hat{\beta} = \frac{2\pi}{\lambda} n_{\text{eff}} - \frac{\pi}{\Lambda}$ and

$$\kappa_{11} = \frac{\omega}{4} \iint \mathbf{E}_\mathbf{1}^*(x,y) \cdot \Delta\epsilon_1(x,y) \mathbf{E}_\mathbf{1}(x,y) dxdy \tag{2.8a}$$

$$\kappa_{12} = \frac{\omega}{4} \iint \mathbf{E}_\mathbf{1}^*(x,y) \cdot \Delta\epsilon_1(x,y) \mathbf{E}_\mathbf{2}(x,y) dxdy \tag{2.8b}$$

$$= \kappa_{21} = \frac{\omega}{4} \iint \mathbf{E}_\mathbf{2}^*(x,y) \cdot \Delta\epsilon_1(x,y) \mathbf{E}_\mathbf{1}(x,y) dxdy \tag{2.8c}$$

$$\kappa_{22} = \frac{\omega}{4} \iint \mathbf{E}_\mathbf{2}^*(x,y) \cdot \Delta\epsilon_1(x,y) \mathbf{E}_\mathbf{2}(x,y) dxdy \tag{2.8d}$$

where $X^* = \mathbb{R}\text{e}\{X\} - i\,\mathbb{I}\text{m}\{X\}$, the complex conjugate of X. $\mathbf{E}_{\mathbf{1,2}}(x,y)$ is the 2 dimensional average field distribution of the mode, calculated with Lumerical MODE in this work. $\Delta\epsilon_1(x,y)$ is the first-order Fourier-expansion coefficient of the dielectric perturbation, $4/\pi$ times the difference between the two dielectric material cross-section for rectangular shaped corrugations.

2.4.1 Mode profiles and dielectric perturbations

The variables $\mathbf{E_1}(x, y)$, $\mathbf{E_2}(x, y)$ and $\Delta\epsilon_1(x, y)$ used in equation 2.8 are illustrated in figure 2.3. This figure shows (x, y) distribution the first two TE modes present in an assymetric coupler and the dielectric perturbation caused by corrugations.

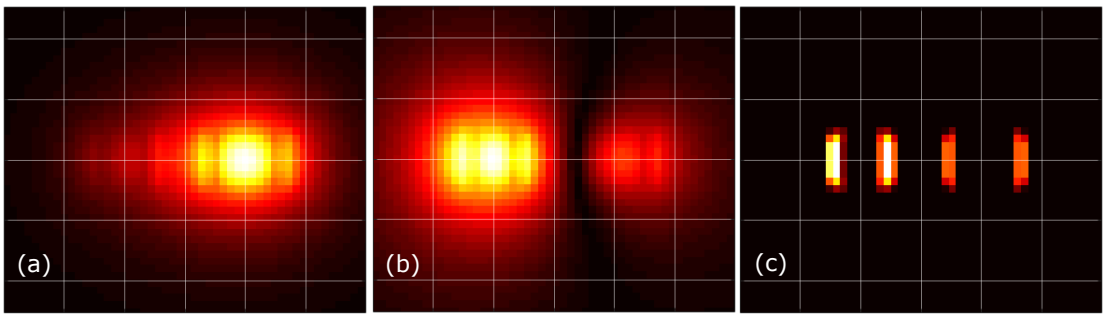

Figure 2.3: Electric field distribution in a) the larger waveguide and b) the narrower waveguide. c) The dielectric perturbation caused by the corrugations.

We observe that the first TE mode is well confined into the larger waveguide, looking much like the TE mode present in an isolated single mode waveguide. The second mode is more localized in the second narrower waveguide, but a non-negligible part of the energy is also in the nearby waveguide. We often call such doubly guided mode a "supermode".

The last picture shows the dielectric perturbation, which is the difference of the cross-section when the waveguides are far apart and closer together (see fig.2.2). While these are in principle rectangular when rectangular corrugations are used, we observe that the edges need to be interpolated when calculated with a coarse mesh size. The integral of equation 2.8 if the sum of all coordinates where these 3 fields overlap. This allows us to visualize that the coupling κ_{12} is proportional to the size of the corrugations, and also that coupling requires the two waveguides to be in close proximity so that the electric fields overlap.

2.5 Simple Response

Using a constant n_{eff} and κ coupling we can calculate the transfer function of the filter, with amplitude and phase components (group delay), shown in figure 2.4. The parameters for this simulation are $\kappa = 30/\text{mm}$, $\Lambda = 260$ nm, $N = 1000$, $n_{\text{eff},1} = 2.7$ and $n_{\text{eff},2} = 2.4$.

We observe that the spectrum is separated in a drop band and a through band. The extinction ratio for the through port is over 40 dB. The out of band suppression for the drop port is lower, with sidelobes around -2 dB, indicating important losses in the through port for these wavelengths. These sidelobes can also potentially interfere with the other channels.

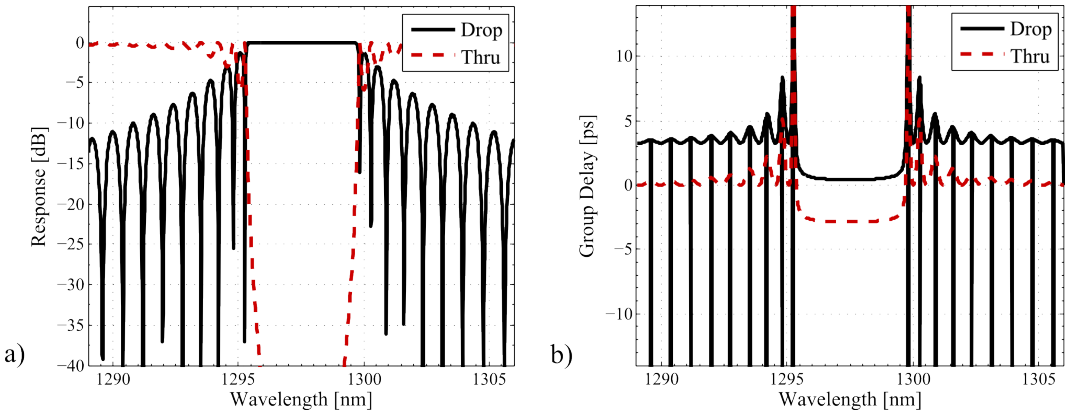

Figure 2.4: Simulated response of a simple uniform contra-directional coupler (a) in amplitude and (b) in phase.

The spectral efficiency of this filter is high due do its square shape, the guard band needed is small compared to the bandwidth. There are many metrics to evaluate this efficiency, such as dB/nm of slope, with merits depending on the application. This study chooses to use the 1-dB bandwidth compared to the 20-dB bandwidth since 1 dB of loss and 20 dB of crosstalk are representative of the typical limits of telecommunication operation.

Figure 2.4b shows the relative group delay over the drop-band. This information is important when sending data because modulated light covers a broad spectrum. All of the components must be synchronized for optimal reception, otherwise inter symbol interference (ISI) is present. An useful number to know is that a 10 GHz baud rate corresponds to a pulse length of 100 ps. The figure shows that the delay is flat within the band, with some ripples under 10 ps of amplitude on the side, meaning that even for high baud rate, pulse dispersion is not an issue except on the sides of the band. Note that the sharp peaks and discontinuities are caused by near-zero signals and are thus not an issue.

2.6 Apodization

The main metric to improve upon with uniform contra-DCs is the sidelobes suppression ratio (SLRL). Sidelobes can be reduced with a technique known as apodization. From the perspective of Fourier transforms, discontinuities to the κ coupling cause sidelobes to appear. Since the coupling is zero outside the grating and non-zero inside, a smooth transition is necessary.

The cross coupling coefficients are dependent on field overlap and the amplitude of the corrugations (see eq. 2.8). We can thus change the coupling by varying the waveguides corrugations.

As the geometry changes, the refractive index along the length also changes, which causes a non-constant resonant wavelength, known as chirp. One should simulate all used cross-sections to ensure that the index is constant in order to suppress unintended chirp. See section 2.7.2

for more detail on coupling related phase noise.

The shape of the coupling profile must ideally follow an infinitely differentiable function such as a gaussian, sine or cosine. These functions are known as window functions and have been previously analyzed in great detail [10]. This study focuses on the truncated gaussian function and on one example of cosine-based function, the Blackman-Nuttall window.

Table 2.1: Figures of merit for different apodizations

Apodization Function	SLSR	1 dB Bandwidth	20 dB Bandwidth	Efficiency Ratio
Rectangular	-2 dB	4.51 nm / 802 GHz	5.04 nm / 896 GHz	89.5%
Gaussian a=1	-17 dB	3.99 nm / 711 GHz	6.33 nm / 1128 GHz	63.1%
Gaussian a=5	-28 dB	3.91 nm / 696 GHz	6.25 nm / 1112 GHz	62.6%
Gaussian a=22	-60 dB	3.66 nm / 651 GHz	6.80 nm / 1211 GHz	53.7%
Blackman-Nuttall	-80 dB	3.70 nm / 658 GHz	6.84 nm / 1218 GHz	54.0%

Figure 2.5 and table 2.1 show the performance for these functions while keeping the maximal coupling constant ($\kappa_{\max} = 30/\text{mm}$). We observe a trade-off of sidelobes suppression ratio (SLSR) against bandwidth and spectral efficiency (defined as $BW_{1\text{dB}}/BW_{20\text{dB}}$). Higher order apodization also cause the central thru port losses to be higher.

While a gaussian function is infinitely differentiable, a truncated one is not, explaining the higher sidelobes. The gaussian used is e^{-ax^2}, is truncated between x = -0.5 and 0.5 and normalized. The a parameter allows the function to be tuned.

We observe that the Blackman-Nuttall cosine window has lower side-lobes than high order gaussians. However, noise present in the system after fabrication is significantly higher than these sidelobes. Thus, it is more flexible to only use gaussian windows and simply tune a for different levels of apodization.

An other comparison that can be done between window functions is to keep the sum of all coupling along the length constant such that $\int \kappa(z)dz = \kappa_{\text{sum}}$. In the case of the uniform rectangular coupling, this is simply $\kappa_{\text{sum}} = \kappa z$. The coupling sum can be kept constant for different window functions by adjusting the length (number of periods) or the maximal coupling. Figure 2.6 shows the obtained response for uniform rectangular, gaussian with $a = 5$ and Blackman-Nuttall window functions. The uniform coupling is decreased to $\kappa_{\max} = 15/\text{mm}$ to better observe the through port losses. Since the area under the curve of a gaussian with $a = 5$ is calculated to be 1.7045 times less than under a rectangle of same height, this is the factor by which the number of period or maximal coupling is adjusted. This factor is 2.7522 for the Blackman-Nuttall function.

We observe that the central through port losses (bottom of the dashed lines) are constant for all of these curves, indicating that it is a function of only κ_{sum} out of these variable. As shown in a), making the device longer with more periods to compensate induces additional total propagation loss . The comparison in b) shows that by increasing $\kappa_{\max}$ to compensate,

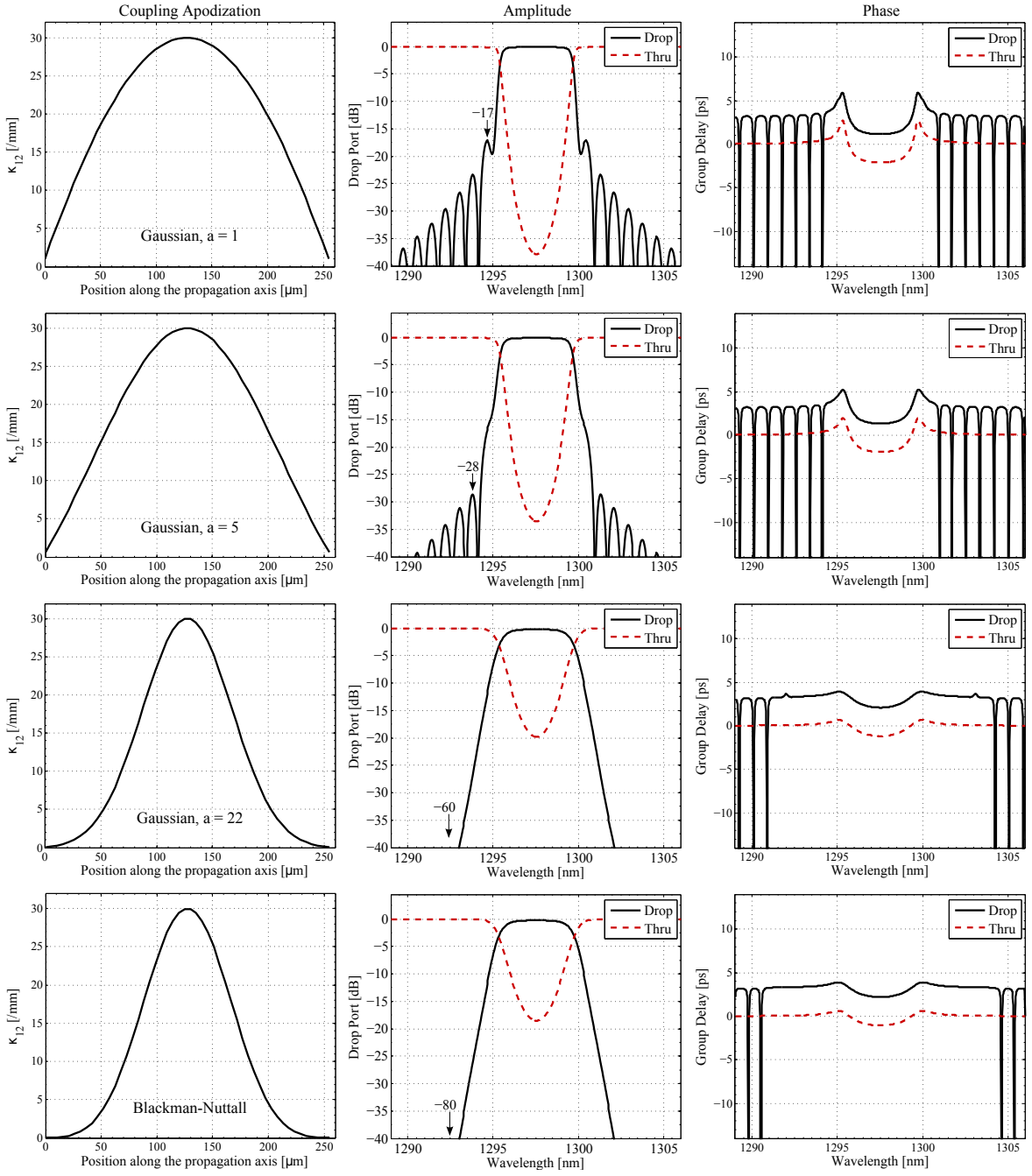

Figure 2.5: Amplitude and phase for various apodization profiles. Each row illustrates a different coupling profile shape and the resulting amplitude and phase response.

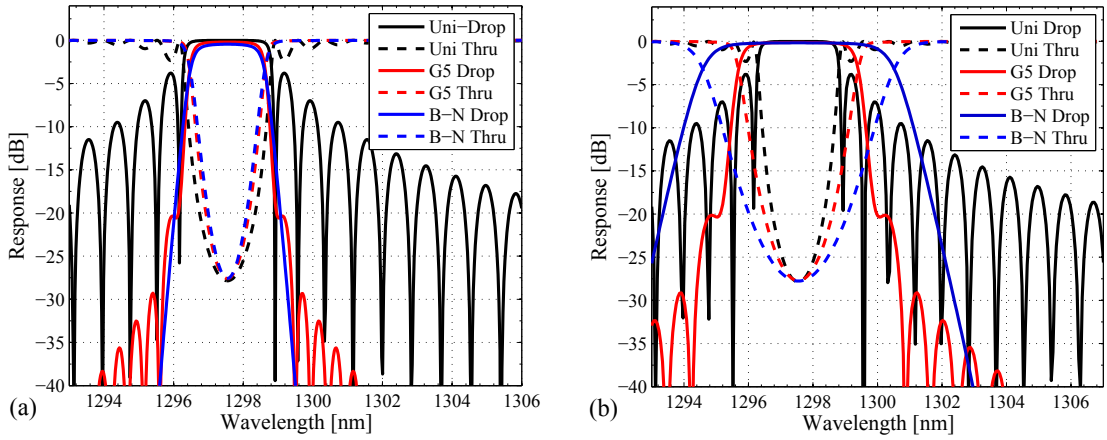

Figure 2.6: Amplitude response for coupling profile uniform, gaussian with $a = 5$ and Blackman-Nuttall while κ_{sum} is constant a) with constant κ_{max} and adjusting the number of periods, b) with constant a number of periods and adjusting κ_{max}.

the bandwidth increases proportionally. Since filters usually have a specific target bandwidth, compensating with increased coupling isn't effective.

Thus, the trade-off is between compensating the length or not. The main metric that affected in both cases is the insertion loss. Too few periods decrease the reflectivity in the drop band, allowing losses by the through port, while too many periods increase the propagation loss due to the device being longer. The insertion loss can thus be optimized to a certain number of periods. A good rule of thumb is to target central through port transmission of around -20 dB, indicating that only 1% of the light is lost through. Long devices however also suffer from more fabrication variance, as seen in section 2.7, so it can be preferable to make devices shorter than this insertion loss optimization would indicate.

This approach is valid for a square shaped filter response. For other purposes, a more general approach such as inverse layer peeling [30] is needed.

2.7 Phase Noise

While the previous simulation results provide important insight into the design of contra-DC, they only explain part of the results measured in the laboratory, for which out of band suppression ratio is limited no matter the apodization profile chosen and other distortions are also observed.

The segmentation of the C matrix allows us to examine variations of coupling coefficient κ along the length for apodization, but also lets us change the propagation constant β as well. This allows us to represent the variation in effective caused by imperfect fabrication. This effectively changes the optical length of each grating element and the corresponding local

resonant wavelength.

Figure 2.7 shows the curve fit of experimental results with this effect added. This is modeled with 3 different sources of distortion causing a fraction of variation to the effective index in both waveguides. It uses the same parameters as before, now with $a = 1$, linear chirp being 0.2% from one end to the other, coupling dependant chirp being 0.1% between the minimum and maximum coupling and random chirp being 0.006% in amplitude.

2.7.1 Random Chirp

The first noise source is from the sidewall roughness. This random change on local index, well known in integrated Bragg gratings [25], is the cause of a noisy transfer function floor, limiting the out-of-band rejection. In order to reproduce it in the simulation, the index is varied randomly within a given amplitude and with white noise distribution over each transfer matrix segment. The spatial frequency of the noise is then, unlike in the real system, equal to the segment length. Since the height of the noise floor is dependent on both the frequency and amplitude of the index change, the noise can be fitted by changing the amplitude.

2.7.2 Coupling Chirp

The second source of distortion is the coupling apodization related index change. While we try our best to have the same effective index all the way along the grating in principle, fabrication can distort small features. This can cause chirp, typically by increasing the index where corrugations are larger. This results in higher sidelobes on one side of the transfer band. This effect can however be compensated in subsequent fabrication runs once the process is known and the small feature distortion can be taken into account in the layout design.

2.7.3 Linear Chirp

An unintended linear chirp can be present across the length of the device. This is usually caused by a slight slope in the thickness of the silicon wafer or by a large scale variation in the lithography or etching in case of optical lithography. We expect a variation of these parameters between the center of the wafer and the edges. This variation, when observed over a short distance, will appear linear. This kind of chirp can be reduced by making the device more localized, e.g. shorter. It would be possible to reduce the distance between the two ends of the grating by curving the device, which has been demonstrated to work with spiral Bragg gratings [29].

2.8 Conclusion

This chapter explained that contra-directional couplers are coupled waveguides with corrugations that can be used to separate wavelength and shown how to calculate their response.

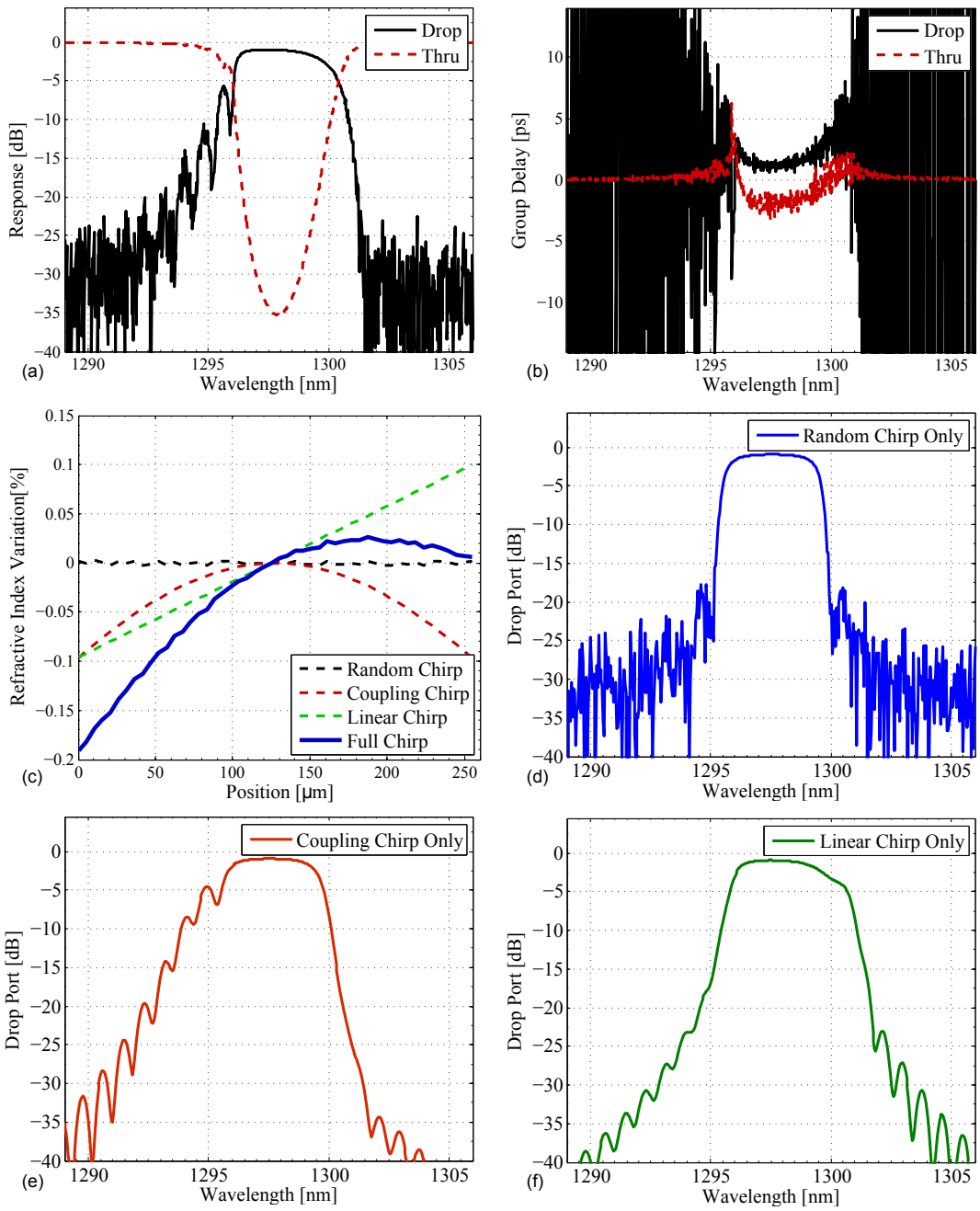

Figure 2.7: a) The amplitude and b) phase responses with all effects considered. c) The effective index variation for the different effects along the length of the grating. d) Amplitude response with only random chirp being considered e) For only coupling depandant chirp f) For only linear chirp.

It is shown that, using segmented matrices, it is possible to accurately simulate apodization and chirp in these devices. This technique can be used to further study the limitations of contra-directional couplers and optimize designs to the fabrication process.

Chapter 3

O-band WDM with deep UV lithography

This chapter was originally presented to OFC 2016 [33]. It was written in collaboration with Sophie LaRochelle and Wei Shi, both contributing to revisions of the article and supervising the project. Wei Shi especially refined the introduction. I was in charge of the design, simulations, measurements and manuscript.

Résumé

Nous démontrons le premier (dé-)multiplexeur basé sur les réseau de Bragg à 4 canaux dans la bande O, fabriqué en utilisant une lithographie à 193nm sur SOI sous-micromètrique, avec des éléments plus petits que 140 nm.

Abstract

We demonstrate the first Bragg-grating-based 4-channel O-band (de-)multiplexer fabricated using 193nm lithography on submicron-SOI with small features below 140nm.

3.1 Introduction

Integrated optical filters are key components for next-generation optical communications systems enabling cloud services, video streaming, and other data-heavy applications. Applying wavelength division multiplexing (WDM) in data centers allows fibers to transport more information, which requires high-performance, low-cost filters and multiplexers that work in the O-band near 1310 nm, where the chromatic dispersion in conventional fibers is minimal. Integrated WDM on the submicron silicon-on-insulator (SOI) platform can be achieved using

lattice filters[12] or arrayed waveguides [18], which, nevertheless, have relatively large footprints and limited free-spectral ranges (FSRs). Others approaches include Bragg gratings[27] and micro-ring filters[38]. However, conventional Bragg gratings work in the reflection mode, requiring circulators or interferometers for add-drop operation. Micro-rings suffer from small FSRs and narrow bandwidths. In addition, most existing SOI filters are in C-band, while O-band may be more important for short-reach applications.

Contra-directional couplers (contra-DCs) are Bragg-grating assisted add-drop filters that offer large bandwidth, flat-top response, compact footprint, and high sidelobes suppression [21]. High-performance coarse WDM using contra-DCs has been demonstrated at 1550 nm using e-beam lithography [24]. It is critical to implement these devices using deep-ultraviolet lithography for mass production, which is challenging since they require small features for gratings [22]. This issue is more significant for 1310 nm applications as the shorter wavelength requires smaller features such as grating pitch and coupler gap.

In this paper, we propose a novel contra-DC geometry in a rib waveguide to increase the mode coupling and thus relax the requirement for small features. The design is implemented using a CMOS-compatible process with 193 nm lithography and a phase-shift mask. We present the first results of a 4-channel Bragg (de-)multiplexer in O-band with high sidelobe suppression.

3.2 Device design and performance

3.2.1 Design

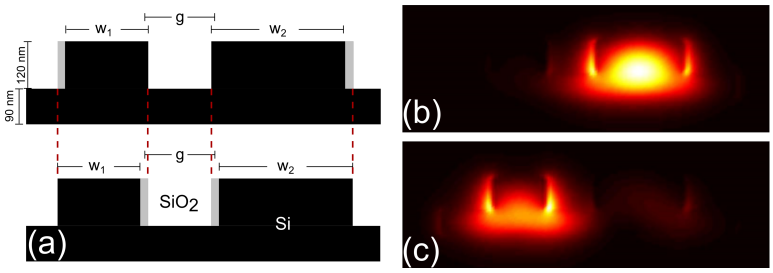

Figure 3.1: a)Schematics of the cross-section over a period when close (top) and far (bottom): w_1 and w_2 are the waveguide widths, and g the average gap. b) and c) Intensity distribution of the first and second supermodes.

The contra-DC filters and cascaded multiplexers are designed for the standard 220-nm SOI wafer. Each contra-DC consists of two waveguides in proximity, with a periodic dielectric perturbations, i.e., Bragg gratings, in the gap region. This introduces wavelength-selective, contra-directional coupling at $\lambda_c = \Lambda(n_1 + n_2)$, where Λ is the grating pitch, and n_1 and n_2 are the effective indices of the first-order and second-order eigenmodes in the coupler. The waveguide coupler is highly asymmetric to suppress the co-directional coupling that would occur with two identical waveguides.

Figure 3.1 shows the schematic cross-section of the proposed structure and simulated mode profiles. We observe that the mode confinement is relatively weak due to the small waveguide widths (220 nm and 360 nm) and the existence of the slab in between. Therefore, there is a much stronger mode overlap with the corrugations, compared to the previously demonstrated device in strip waveguide. This allows for stronger coupling, which enables a large bandwidth with a relatively large feature size. The contra-DCs are apodized to reduce side-lobes using a gaussian profile in the coupling with an apodization index $a = 10$, following the method described in [21].They have 1000 corrugations, measure 400 µm long and 5 µm wide.

3.2.2 Fabrication

The fabrication was performed using a CMOS compatible silicon photonic process with deep UV (193 nm) lithography at IME, Singapore. A phase shift mask is applied, which allows high precision for small features such as grating corrugations. Figure 3.2 b) shows the SEM image of a device on a separate wafer without oxide cladding. We can see clearly see the grating corrugations, even though the square shaped corrugations in the layout design are smoothed in the lithography as expected. Corrugations with a small period of 260 nm and gaps under 140 nm are resolved. However, the width of the waveguide along the coupling apodization profile is uneven due to the approximation effect in optical lithography. This results in effective index variations along the propagation direction and thus distortion of the apodization profile, as seen in the measured spectra to be discussed below.

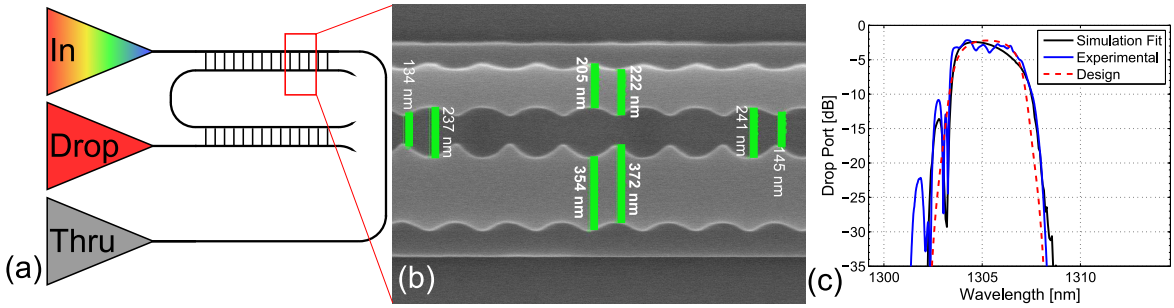

Figure 3.2: a) Schematic of a dual-stage single-channel contra-DC. b)SEM showing that the waveguide widths vary in the close and far regions. c) Simulated and measured spectral response of the dual-stage contra-DC, with fiber-to-chip response subtracted.

3.2.3 Experimental results

Figure 3.2 c) shows the spectral response of a dual stage filter. The insertion loss is 2.5 dB with a 1-dB bandwidth that covers 370 GHz. A sidelobe suppression ratio of 8 dB is obtained, which is lower than the results ($>$ 20 dB) achieved with the devices fabricated using e-beam lithography [24]. This is explained by the variations in corrugations and effective indices due to fabrication errors. As a result, the effective indices in the strong coupling regions are higher

than in the weak coupling regions, which creates undesired coupling dependent chirp, i.e., phase distortion along the grating apodization profile. Taking this coupling dependent chirp into consideration, our simulation fits well with experimental results. With this information, we will be able to bias future devices to compensate for the optical lithography impact and significantly improve the performance.

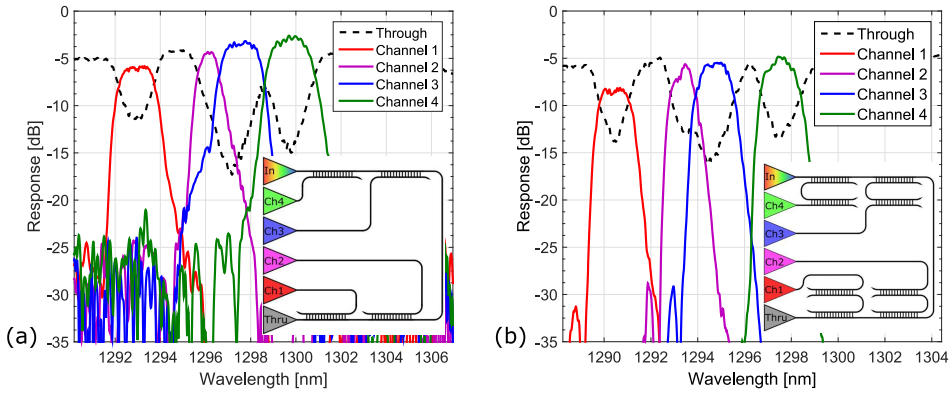

Figure 3.3: Measured spectra of contra-DC demultiplexers: a) single-stage; b) dual-stage.

Figure 3.3 shows the performance of two 4-channel wavelength demultiplexers. The device (Fig. 3.3a) consists of four contra-DCs cascaded along a bus waveguide. The second one (Fig. 3.3b) applies dual-stage filtering for a lower crosstalk. The contra-DCs in different channels have slightly different pitch (Λ) for specific wavelengths. The channels are dropped in a reverse order such that shorter wavelengths go through more contra-DCs and thus have a longer waveguide path to traverse. This explains why the loss increases as the channel wavelength decreases. An obvious problem is that the second channel has a smaller bandwidth than the others and its center wavelength is off the design grid. We believe this is due to the quantization errors in the grating pitch definition in the mask layout and should be avoided in the future using precise control of the center wavelength by varying the waveguide widths instead of pitch. Simulation shows that increasing the average index in the gratings of channel 2 by 0.1% causes this behavior. As shown in Fig. 3.3b, other channels without suffering from this error have shown good performance with a low crosstalk below -25 dB.

3.3 Conclusion

In summary, we demonstrated, for the first time, Bragg-grating-based multiplexers in the O-band on submicron SOI using UV lithography. This technology is a key enabler for low cost and flexible WDM in data centers. The prototype presented gives the community critical information about the possible issues when using UV lithography for small features and how to consider them for future designs.

Chapter 4

Cascaded tunable filter

This chapter was originally published in Optics Letters Vol. 40, Issue 23, (2015) [32]. It was written in collaboration with Sophie LaRochelle and Wei Shi, both contributing to revisions of the article and supervising the project. Hadi Bahrami laid out the device and Philippe Jean assisted in the measurements. I was in charge of the measurements, analysis, modeling and writing of manuscript.

Résumé

Les réseaux optiques à haute capacité de nouvelle génération nescéssitent une allocation flexible des ressources spectrales, pour laquelle des filtres optiques bon marché avec une grande accordabilité de plusieurs centaines de GHz sont désiré Nous démontrons un filtre passe-bande intégré avec une bande passante accordée de façon continue sur 670 GHz (117 GHz à 788 GHz), qui, selon le meilleur de nos connaissances, est la plage d'accordabilité la plus large jamais démontrée sur une puce de silicium. Le filtre offre aussi la capacité d'accorder la longueur d'onde ainsi qu'une plage de spectre libre illimitée. Nous avons mesuré un contraste hors-bande de 55 dB, de faibles variations à l'intérieur de la bande de 0.3 dB, et une variation du délai de groupe dans la bande de moins de 8 ps. Ce résultat fût réalisé en utilisant des coupleurs contra-directionels cascadés et des micro-éléments chauffants sur la plateforme de silicium sur isolant de 220 nm, avec une surface de moins de 7 000 μm^2. Un autre design avec la bande passante accordable de 50 GHz à 1 THz est présenté.

Abstract

Next-generation high-capacity optical networks require flexible allocation of spectrum resources, for which low-cost optical filters with an ultrawide bandwidth tunability beyond hundred GHz are desired. We demonstrate an integrated band-pass filter with the bandwidth continuously tuned across 670 GHz (117 GHz to 788 GHz), which, to the best of

our knowledge, is the widest tuning span ever demonstrated on a silicon chip. The filter also features simultaneous wavelength tuning and an unlimited free spectral range. We measured an out-of-band contrast of up to 55 dB, low in-band ripples of less than 0.3 dB, and in-band group delay variation of less than 8 ps. This result was achieved using cascaded Bragg-grating-assisted contra-directional couplers and micro-heaters on the 220-nm silicon-on-insulator platform with a footprint of less than 7,000 μm^2. Another design with the bandwidth continuously tunable from 50 GHz to 1 THz is also presented.

4.1 Introduction

Next-generation optical transmission systems applying flexible networking and the super-channel technique will require highly dynamic channel allocation to drastically increase the spectral efficiency and transmission capacity [13, 8]. Tunable optical filters, reconfigurable in both center wavelength and bandwidth with scalability towards terahertz [8], are essential for these applications. Such large bandwidth tunability is currently only available in bulky bench-top systems using diffractive grating spectrometers or liquid crystals. Integrated solutions are desired for lower cost and power consumption. In particular, silicon photonics based on the sub-micron silicon-on-insulator platform allows for CMOS compatible mass fabrication, enabling low cost, high yield, and high-density chip-scale integration. Existing solutions for tunable filters on silicon include devices based on microring resonators [40, 19] and Mach-Zehnder interferometers (MZIs). These devices have relatively small tunable bandwidth (less than 200 GHz) and small free spectral range (FSR) – typically less than 10 nm, unable to cover the entire C-band, which are not suitable for high-capacity transmission applications.

Contra-directional couplers(contra-DCs) are grating-assisted add-drop filters [21]. Analogous to waveguide Bragg gratings, the wavelength selectivity in contra-DCs is based on periodic dielectric perturbations. But instead of back-reflections in the same waveguide, the selected wavelength in a contra-DC is dropped to another waveguide through contra-directional coupling. This allows add-drop operation without the need of a circulator. Contra-DCs have merits of compactness, flat-top response, flexible filter design (e.g, through apodization), and near-infinite FSR (in the case of first-order gratings). In particular, they allow for very high bandwidths (greater than 10 nm) and thus can support very-high-baud-rate super-channel signals [13]. In this paper, we demonstrate a broadband filter with a large tunability in both wavelength and channel bandwidth, using thermally controlled cascaded contra-DCs on a silicon chip. The filter has flat-top responses, low insertion loss, low in-band ripples, and high contrast between the pass-band and the stop-band.

4.2 Principle and Design

The schematic of the proposed device is shown in Fig. 4.1. It consists of a pair of cascaded contra-DCs, each operating as a drop filter. The drop port of the first contra-DC is connected

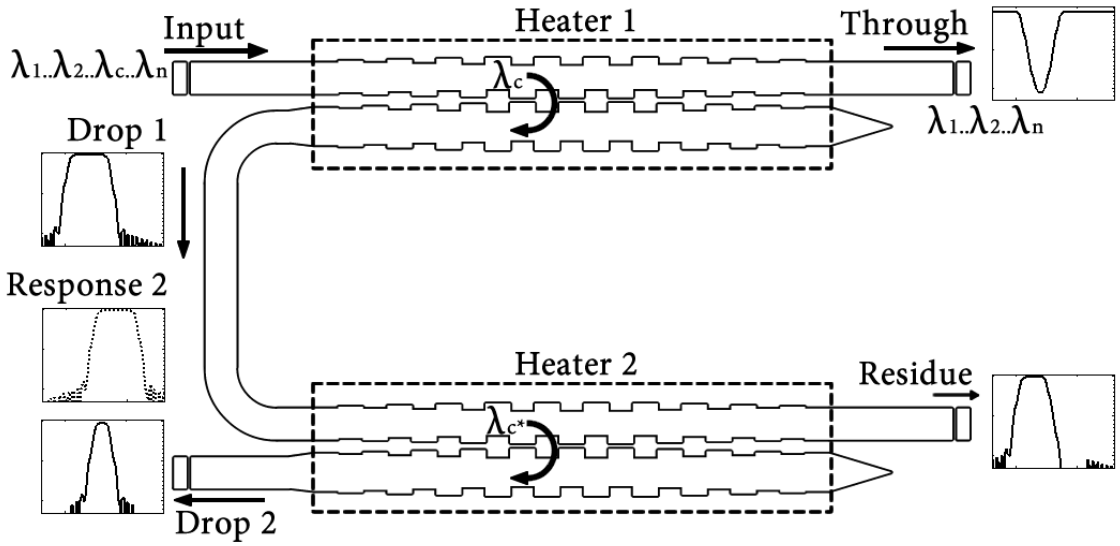

Figure 4.1: Schematic of the device. The dropped wavelength of the first contra-directional coupler is re-filtered in an identical component. Both contra-directional couplers are temperature-controlled with metal heaters. Plots show examples of spectrum at each port, on a logarithmic scale.

to the input port of the second contra-DC. Therefore, the finally dropped signal("Drop port of the system"), is determined by the product of the drop-port transfer functions of the two contra-DCs.

At first, the two filters are identical and drop a large, well-defined window. By changing the temperature of a single filter, the bandwidth of the finally dropped signal can be adjusted by detuning the center wavelengths of the two contra-DCs.

A broadband filter design for a coarse WDM on the 220-nm SOI platform [24] is adopted for individual contra-DCs. In each contra-DC, the widths of the waveguides are 560 nm and 440 nm. This high asymmetry ensures a negligible forward cross-coupling. The gratings are formed by sidewall corrugations in strip waveguides with a pitch of 312 nm. Each contra-DC has 1,000 grating elements for a length of 312 µm. The spacing between the waveguides varies between 65 and 135 nm to produce a Gaussian-profiled coupling apodization as shown in Fig. 4.2 for efficient sidelobe suppression, for which details can be found in [24].

The spectral responses of each contra-DC is calculated using coupled mode theory and the transfer matrix method, following the same procedure as in [21], with three additions: apodization, temperature dependence and noise simulation. While an unapodized (uniform) grating can be simulated with only two transfer matrices, an apodized design needs an independent matrix for each grating element along the propagation, to match the change of coupling, and the transfer matrix of the entire contra-DC is given by the product of all the grating elements along the propagation axis. Our simulations use 100 segments to approximate the continuously

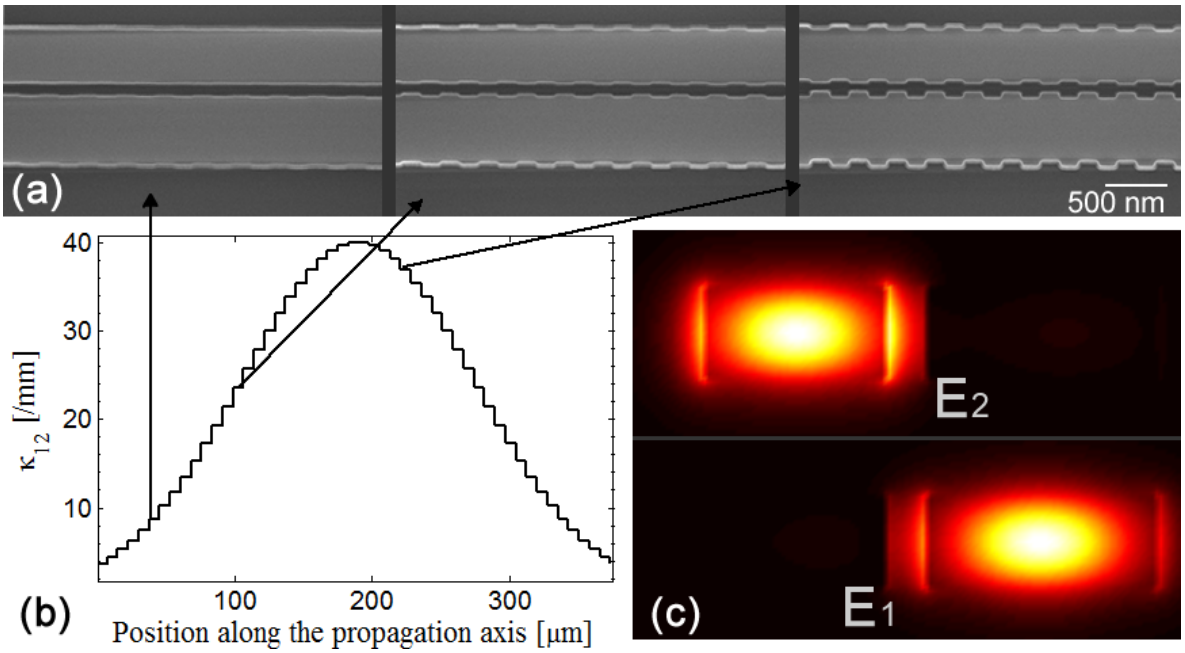

Figure 4.2: (a)SEM photography of a part of the grating. The contra-directional coupler consists of two close waveguides of different width with periodic sidewall corrugations. (b) Apodization profile of the grating. A larger coupling requires larger corrugations. (c) Intensity distributions of electrical fields of the first and second transverse modes.

varied coupling.

On top of each contra-DC sits a metal strip acting as a micro-heater for thermal tuning. The refractive index of silicon has a temperature dependence of $\mathrm{d}n_{\mathrm{Si}}/\mathrm{d}T = 1.87\times10^{-4}\mathrm{K}^{-1}$ at room temperature for wavelengths around 1550 nm [7]. Without electrical input, the optical responses of the two filters are in principle identical (except for fabrication errors), resulting in a sharp transition from the pass-band to the stop-band. Applying independent electrical currents on the heaters, we can shift the spectra of the contra-DCs simultaneously or differentially for wavelength or bandwidth tuning. Ideally, each contra-DC should be uniformly heated so that the apodization profile would not be disturbed as the temperature varies. In simulation, the temperature dependence is accounted for by $\mathrm{d}n_{\mathrm{eff}} = \mathrm{d}n_{\mathrm{Si}}/\mathrm{d}T \times \mathrm{d}n_{\mathrm{eff}}/\mathrm{d}n_{\mathrm{Si}} \times \mathrm{d}T$, where $\mathrm{d}n_{\mathrm{eff}}/\mathrm{d}n_{\mathrm{Si}}$ is evaluated using an eigenmode solver.

While only coupling apodization has been discussed so far, it is common in Bragg grating profiles to also adjust the local Bragg wavelength. This can be done with a phase shift changing the local effective index or period. This design only uses coupling apodization in principle, but phase noise also appears during fabrication due to non-uniformity and sidewall roughness.

There are two main types of waveguide noise considered in our simulation. High-frequency phase noise (typically around 10 μm of spatial period [26]) is caused by sidewall roughness

and decreases the sidelobe suppression. Low-frequency phase noise, with a correlation length larger than the device (300 µm), is caused by the wafer thickness non-uniformity and etching variance, resulting in a linear chirp that increases the bandwidth. High frequency phase noise is considered in our simulation by adding random noise $\Delta\hat{\beta}$ to the propagation constants. The frequency distribution of the noise thus matches the quantization steps of the matrices, but since the response noise is dependent on both the amplitude and frequency of the sidewall roughness [25], we can fit the simulation to the experiment by choosing the right noise amplitude. Similarly, we can also add a variation to $\Delta\hat{\beta}$ which is dependent on the longitudinal position.

4.3 Experiment

The device was fabricated using a CMOS-compatible technology with electron-beam lithography. Large coupling coefficients and precise apodization profiles are easier to achieve with this process, although optical lithography able to resolve the required periodicity and gap between waveguides as seen in 4.2 a) could be used. The corrugations do not need to be square shaped, but must have a large enough amplitude . Fiber grating couplers [42] are used as optical inputs and outputs in the measurement. Fig. 4.3 shows the measured drop port response of the cascaded contra-DC filters. The measurements were normalized using the response of a pair of directly connected fiber grating couplers on the same chip.

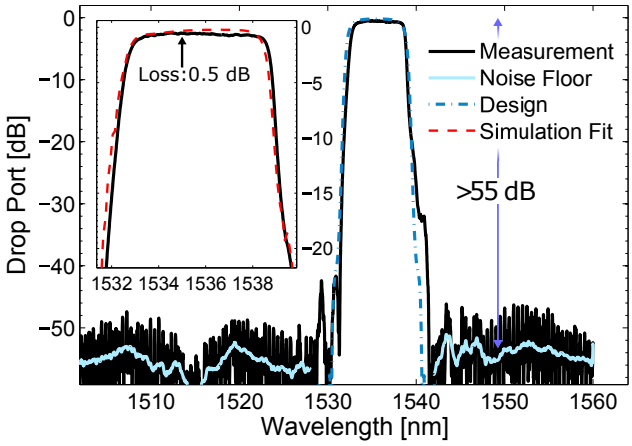

Figure 4.3: Spectral response of the cascaded filters without heating: 1-dB BW is 733 GHz, 3-dB BW is 788 GHz, 10-dB BW is 868 GHz, and 20-dB BW is 990 GHz. Inset shows the filter shape up to -20 dB, which is the typical communication requirement.

The device exhibits a high side-lobe suppression ratio (SLSR) of over 40 dB and a high contrast of about 55 dB between the pass-band and the stop-band. The insertion loss is very low, less than 0.5 dB (i.e., 0.25 dB per contra-DC), with small ripples of less than 0.3 dB

within the 1-dB passband over 5.8 nm (733 GHz). This agrees with the measurements in the literature [3]. The edge roll-off rate is 19 dB/nm on the left side and 24 dB/nm on the right side. The simulation agrees well with experiment. The parameters found with a curve fit are $a_{\text{gaussian}} = 10,\ \kappa_{\max} = 37964/\text{m},\ lch = -2.64 * 10^{-3},\ rch = 3 * 10{-}5,\ N = 1000$ for the first filtering stage and $lch = -0.95 * 10^{-3}$ for the second stage.

4.3.1 Phase

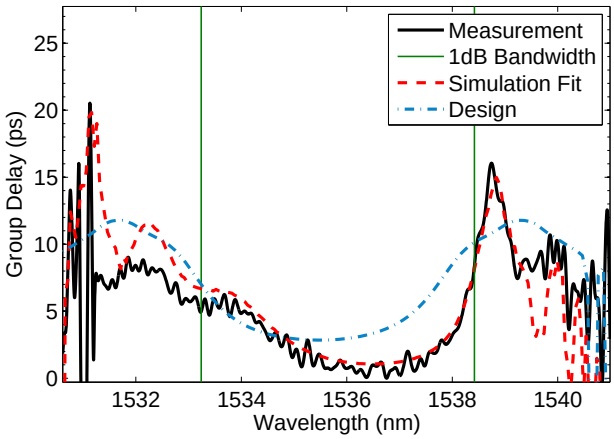

Figure 4.4: Group delay response of the tunable filter at the drop port. The delay stays within 8 ps between any two points in the band. The out of band results are noisy due to the weak signal.

Another important parameter to monitor is the group delay, as an uneven delay within the pass band may cause signal distortion. The simulation and measurements seen in Fig. 4.4 both show a group delay difference of less than 8 ps within the 1-dB bandwidth. Compared to the original design without considering the phase noise due to fabrication errors, the measured group delay shows a slight distortion. Good agreement is obtained by taking into consideration the linear chirp caused by the silicon wafer thickness variation, estimated through curve fit.

Further work could be done to optimize the grating structure further using the inverse layer peeling algorithm[30] since the mathematics of the contra-directional coupler are similar to those of Bragg gratings.

By changing the temperature of a single contra-DC, we shift its phase-match condition, resulting in a smaller band overlap between the two contra-DCs and thus a narrower passband in the drop port, as shown in Fig. 4.5. Due to the wavelength detuning, the stop-band edges are now determined by the single filters. As a result, the side-lobes suppression for small bandwidths degrades to -15 dB. A continuous tuning of the 3-dB bandwidth from 788 GHz down to 117 GHz (i.e., over 670 GHz or 5.4 nm) is experimentally observed as the on-chip temperature increases by 70 degrees.

The microheaters are made of 300-nm-thick, 2-µm-wide Al strips. The power efficiency of the bandwidth tuning is about 24 mW/nm, which dissipates a lot of heat and would be impractical for integration with electronics. We also observe a slight red-shift of the center wavelength at higher temperature, indicating thermal coupling between the two contra-DCs that are about 10 µm away from each other. These issues can be resolved by optimizing the heater design, e.g., using smaller heater features and thermal isolation [5].

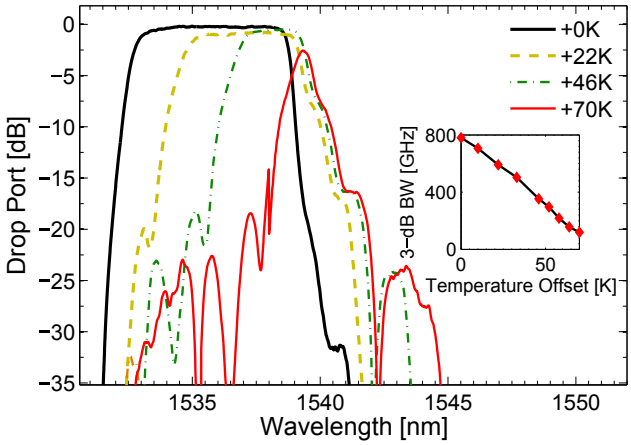

Figure 4.5: Spectral response of the device for different temperatures applied to only one contra-DC: 1-dB BW tuned down to 65 GHz, 3-dB BW to 117 GHz. The temperatures are obtained from simulation fit. Inset shows the temperature dependence.

By applying the same temperature variation on both contra-DCs, the center wavelength can be tuned without affecting the filter shape. As shown in Fig. 4.6, when the center wavelength is continually changed over 4 nm by varying the on-chip temperature, the filter shape is maintained with sharp edges. The power efficiency of the wavelength tuning is about 44 mW/nm, which is about twice the power consumption of the bandwidth tuning since two contra-DCs are heated simultaneously.

Table 4.1: Recent results with multi-element on-chip silicon filters

Publication	Filter type	BWmax / FSR	Tunable BW	On-chip loss / Ripples	Contrast
Ding (2011)[4]	MRs + MZI	55 GHz / 1 THz	28-55 GHz	3.6 dB / 1 dB	30 dB
Orlandi (2012)[20]	MRs + MZI	173 GHz / 200 GHz	23-173 GHz	0.46-1.06 dB / 0.5 dB	15-34 dB
Ong (2013)[19]	Cascaded MRs	125 GHz/ 0.9 THz	11.6-125 GHz	0.25 dB / 3 dB	50-100 dB
This experiment	Cascaded contra-DC	778 GHz / Unlimited	67-778 GHz	0.5 dB / 0.3 dB	15-55 dB
4-stage design	Cascaded contra-DC	1 THz / Unlimited	49-1007 GHz	<1 dB / 0.3 dB	>49 dB

Table 4.1 shows a comparison of recent publications of tunable optical filters on the SOI platform. Our device shows the highest tunable bandwidth and is the only one that allows for a bandwidth beyond 200 GHz. It is noteworthy that the other devices all have a small FSR less than the span of the C-band (35 nm), while our device does not suffer from a limited FSR.

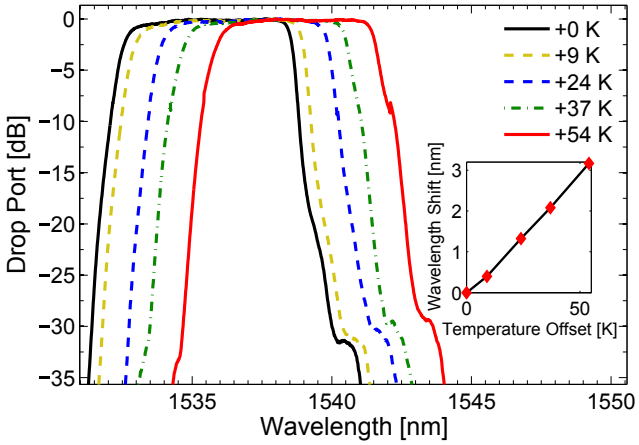

Figure 4.6: Spectral response with the heat applied to both contra-DCs: the central wavelength is tuned from 1535 nm to 1539 nm continuously; the temperatures are calculated by comparison to simulation. Inset shows the temperature dependence.

This indicates a unique capacity for dynamic allocation of spectrum resources. In addition, our device is among the best in terms of loss ripples and contrast.

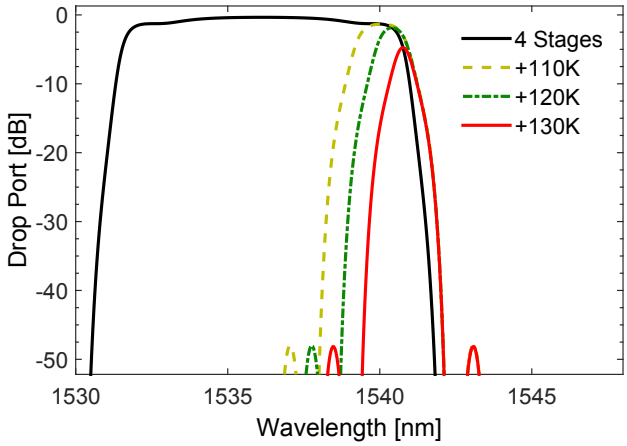

Figure 4.7: Simulation of the spectral response with the heat applied to two out of four cascaded contra-DCs: the 1 dB bandwidth can be continuously tuned from 1007 GHz to 49GHz. The sidelobes stay under -49 dB even for small bandwidths due to the double filtering. This simulation doesn't consider fabrication phase noise.

For improved performance and flexibility, more stages can be cascaded. Fig. 4.7 shows our simulation results of a 4-stage cascade contra-DC filter, consisting of two pairs of identical contra-DCs with a stronger coupling than the one experimentally demonstrated (53.5 mm^{-1} vs 38 mm^{-1}). Each pair is controlled by the same temperature, performing as a single tuning element.

4.4 Conclusion

In summary, we have demonstrated a bandwidth tunable filter with a low insertion loss of less than 0.5 dB, low ripples of less than 0.3 dB, a large maximal bandwidth of greater than 750 GHz, and high contrast of 55 dB. A large bandwidth tuning range over 670 GHz has been achieved, which, to the best of our knowledge, is the widest ever demonstrated on a silicon chip. This ultra-wide bandwidth tunability makes the device very attractive for next-generation ultrahigh baud-rate applications (e.g., high-capacity super-channel transmissions) and flexible optical networking.

Chapter 5

Laboratory measurement of SOI optical devices

The goal of laboratory measurements is to evaluate the performance of optical devices once fabricated. In general, this requires the following steps:

1. Align the optical input and output. This usually involves 2 or more fibers aligned with fiber grating couplers or edge couplers.
2. Measure the spectral response. Sweeping the laser over a certain spectrum and measuring the transmission provides key information, especially for optical filters.
3. For devices with electrical inputs, place the electrodes on the contacts and measure the spectrum for different electrical inputs.
4. (Optional) for filters: Measure the phase response/group delay using an optical vector analyzer (OVA) from LUNA.
5. (Optional) for modulators: Measure the electro optic response S_{21} with a vector network analyzer (VNA). Run a transmission experiment with all the equipment required to drive the modulator at high speed and a bit error rate tester (BERT). This will not be explained further, but details can be found in the equipments manuals.

Since the optical alignment has a lot of particularities and is required to perform the other steps, it will be the main focus of this chapter.

5.1 The optical path

Figure 5.1 shows the path commonly used by light during a test. Light comes in from an external laser through an optical fiber aligned with a fiber grating coupler. The optical circuit

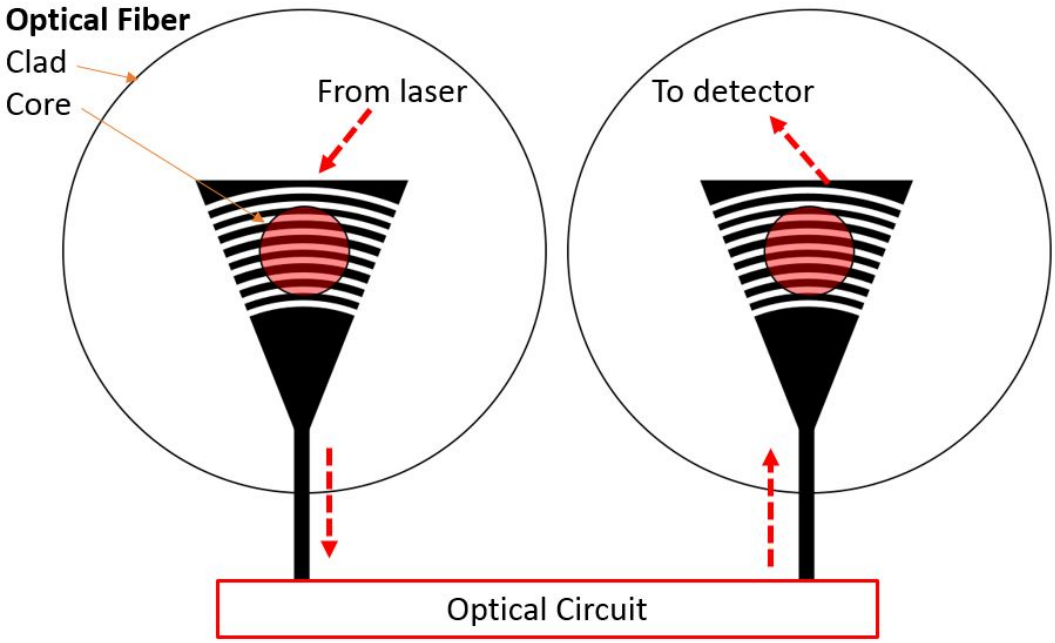

Figure 5.1: Schematic of the path light needs to travel through when testing a device using a pair of fiber grating couplers.

performs a function on this light and the light then exits through a second grating coupler to be detected.

5.2 Fiber grating couplers usage

Fiber grating couplers have three parameters that must be respected:

1. Target *wavelength*. FGCs will only work around a specific wavelength, with a 3-dB window of about 30 to 50 nm. Measurements in different bands require different FGC designs. Figure 5.2 shows typical responses.

2. Target *polarization*. FGCs either interface from a vertical fiber polarization to the silicon TE mode or from an horizontal fiber polarization to the TM mode. The laser is by default linearly polarized and the polarization is preserved to the chip using a polarization maintaining (PM) fiber. A polarization rotator might be required to match the FGC.

3. Target *angle*. The FGC is made to work at a very specific light incidence angle. The fiber array must be rotated properly. Deviations from this angle will reduce maximum transmission and offset the central wavelength.

These parameters are usually indicated in the name of the device such as

TE_1550_220_150_20d_oxide

where TE, 1550 and 20d are the polarization, the wavelength and the angle, respectively. 220 and 150 are the two silicon thicknesses used and oxide specifies that the grating is to be covered with silicon oxide (glass) on top, the alternative being to not be covered, in which case _air is used.

Note that all of these are targets. Since the process, especially the thickness, is not always precise, the final central wavelength can be a few nanometers off. Figure 5.2 shows the responses with a wavelength sweep and on the camera for a few different grating designs.

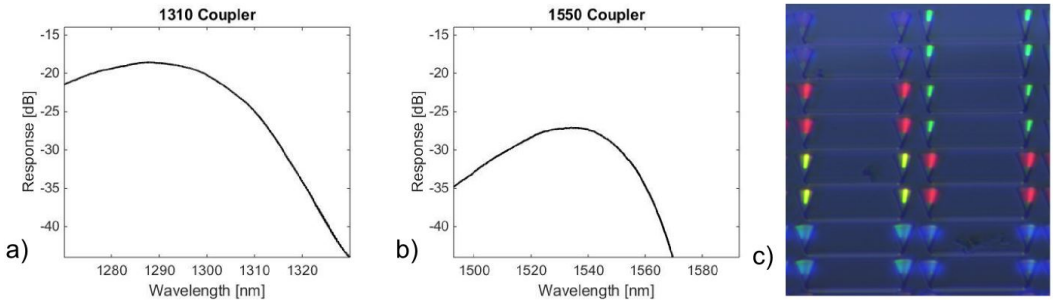

Figure 5.2: Exemple response of a pair FGC at 1310 (a) and 1550 (b). c) Multiple pairs of FGC for different angles, polarization and wavelength as seen on camera.

5.2.1 Fiber arrays and incidence angle

In order to have a good transmission, the fiber must be as close as possible to the chip, usually under 30 µm. Since the glass block holding the fibers in an array is quite thick and the fiber must usually inject at an angle, the fiber array must have a pointy tip so that the back of the glass block doesn't prevent the fiber from getting close enough.

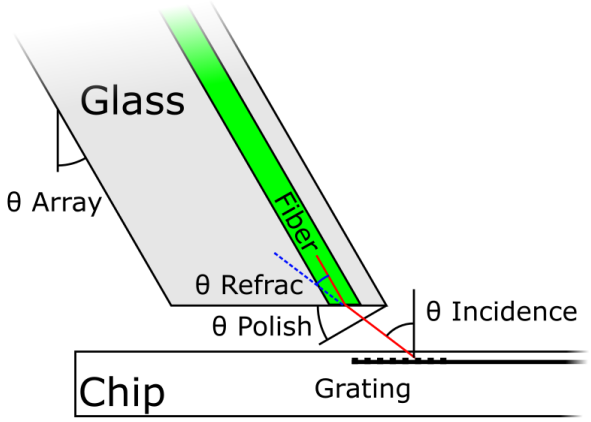

Figure 5.3: The different angles involved in FGC injection with a polished fiber array

Figure 5.3 shows the usual solution to achieve angled injection. The whole surface of the tip, including the fiber, is polished at an angle (θ_{polish}). In addition to allowing the array to move up to a greater θ_{array} without touching, this polish also refracts the light, giving it an additional angle corresponding to θ_{refrac} using Snell's Law:

$$\theta_{\text{refrac}} = \arcsin\left(\frac{n_{\text{glass}}}{n_{\text{air}}}\sin(\theta_{\text{polish}})\right) - \theta_{\text{polish}} \tag{5.1}$$

In the end, $\theta_{\text{incidence}} = \theta_{\text{array}} + \theta_{\text{refrac}}$. Once you know the additional angle provided by refraction, you simply need to place the array at $\theta_{\text{incidence}} - \theta_{\text{refrac}}$. To shortcut the calculation, the refraction angle is provided for standard polish angles in table 5.1.

Note that for negative angles, the procedure is the same, but the chip should be rotated 180°so that the waveguides go the opposite direction (towards the left in Fig. 5.3).

Table 5.1: Angle to substract from grating incidence to get the right angle for the array.

θ_{polish}	10°	20°	24°	28°	32°
θ_{refrac}	4.1°	8.6°	10.7°	13.1°	15.9°

For instance, with a target angle of 20°and a polish angle of 24°, one should angle the fiber at $\theta_{\text{array}} = \theta_{\text{incidence}} - \theta_{\text{refrac}} = 20° - 10.7° = 9.3°$ from vertical.

5.2.2 Grating couplers and polarization

Optical fibers do not normally conserve polarization. Both of the linearly polarized modes are degenerate, with the same propagation constant, and couple to each other. On a given path, the end polarization is predictable, but any new bend or vibration will make it fluctuate.

In order to decouple the modes, the fiber must be made birefringent. A common principle is to place a different material that will cause stress in one direction, but not in the other. Figure 1.5 shows the cross section of such a fiber, called a polarization maintaining (PM) fiber. PM fibers usually have have a blue coating instead of the regular yellow one to help their identification. All of the connection between the laser and the FGC is made of PM fiber, and the laser is linearly polarized in the right direction at his output.

The only point of contention happens when shifting from TE to TM input. In this case, the linear polarization must be rotated 90°. The easiest way to do this precisely in fibers is to use a PM fiber with a 90 °splice in it, where the fast birefringent axis is aligned with the slow axis.

It can be confusing to figure out if the polarization is right during use because some fiber arrays default to TE and other to TM. If the signal is very weak or inexistent when everything looks aligned properly, switching the fiber to rotate the polarization might solve the issue.

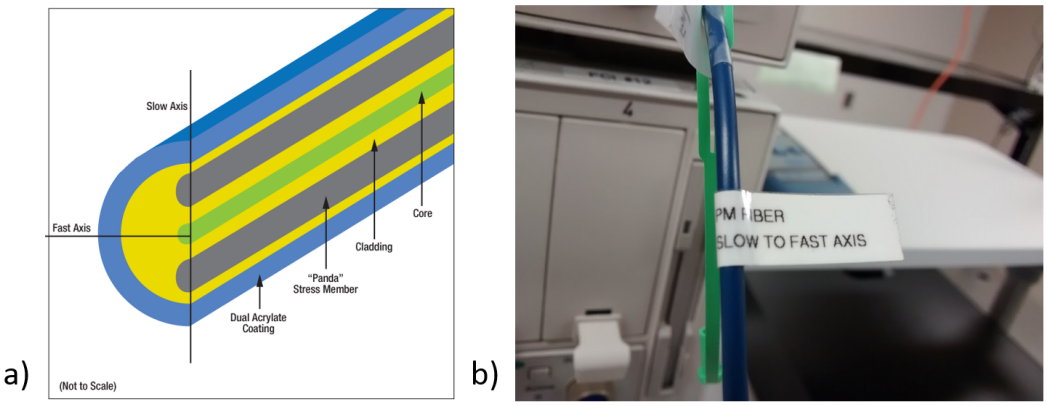

Figure 5.4: a) The cross-section of a birefringent PM fiber.[Thorlabs] b) The slow to fast PM fiber has a label indicating so.

5.3 Optical alignment

On our current setup, optical alignment is performed with precise motors by moving the chip in the X,Y plane, and the fiber arrays moves up and down on the Z axis. Angles are adjusted manually.

The alignment is done in 3 steps of increasing precision:

1. The chip is placed on the test bench with optical inputs facing the array. The chip is moved under the fiber array and the fiber array is moved down by looking at it directly without camera so that it is about 1 mm over the chip.

   The top and front cameras are then adjusted to have a clear view of the fiber array. The angles of the chip surface and of the fiber array are adjusted with the help of cameras. Lighting intensity and angle is adjusted to see has many features as possible, especially the grating couplers. We call this mounting the chip. After this point, only motorized controls are necessary.

2. An alignment mark device (see section 5.3.2) is located on the chip layout and the connected fibers of the array are placed on top of it at an height of 30 µm. While the position of the grating is clearly visible in good lightning, the position of the fibers in the glass block can be hard to evaluate and thus this alignment is approximate. This is the manual coarse alignment.

3. The software moves the chip under the fiber to scan the area quickly and produces a map of transmission points. The map shows a point for each pair of grating coupler and can be compared with the layout to confirm the location. When a pair is found, it can be moved to using the software. Then, a Fine Align function must be executed to finish the X,Y alignment. This is the final automatic alignment.

Angles

There are several angles to adjust on both the optical stage and the fiber array. These steps must be performed when mounting the chip, before light injection is attempted.

1. Adjust the array angle (see section 5.2.1). This is adjusted on the back of the fiber array support. Beware that the height of the array will change a lot when adjusting the angle.
2. Make the chip surface parallel to the movement plane. When moving the chip around, the chip surface should stay at exactly the same height on the camera, even over large distances. If this is not the case, the angles can be adjusted with screws on the corners of the stage.
3. Make the fiber tip parallel to the chip. When moving the fiber array low, both corners of the array should be at the same distance from the chip. This can be adjusted by rotating the array on its screw.
4. Make the fiber tip parallel to the row grating couplers. Light usually needs to enter two or more FGC at once, so the fibers must be in the same as the FGCs. To adjust this, rotate the top of the stage with the rotary mount when the fiber tip is close to a row of gratings.

5.3.1 Alignment using software

The motors, laser and detector are controlled by a computer using a Matlab graphical software created by integrated optics students of several universities.

To set it up, make sure all the peripherals are physically connected and ready. Open the testbench_main.m script, go to the Intr tab, connect everything, go to the Register tab and start the Manual Coordinate Control. The Manual Coordinates Control has all the controls needed for manual measurements of devices, including control for the laser, detector and motors.

Fiber positioning

Each of the fiber in the array is numbered. Numbers on the connectors indicate which fiber is connected. On the camera, when the fiber is coming from the top, fiber number 1 is the rightmost one, proceeding left for higher numbered fibers.

Even knowing the number, it can be difficult to see and locate the fiber since it is underneath a glass cover. In this case, we suggest using the middle fibers (for instance fiber 4 and 5 for an array of 8), which are always in the middle of the array.

Position the pair of fibers at an height of 30 µm over the inputs of the device to test. The center of the fiber is 200 µm from the edge of the array, so the array must overlap over the device by that distance.

Map GC

After manually positioning the fibers, the Map GC function should be used to scan the surface for transmission. This function sends light through the fiber and measures the response on the detector while moving the chip beneath the fibers.

First, check the settings of Map GC. Important parameters are the width X and width Y of the area to scan. These decide the size of the surface being scanned, with the center being the current position. The bigger the widths, the longer the map will take. A typical size when starting is 1000 by 600 (the software unit is µm).

Once the settings are set, run the Map GC. After a few minutes of scanning, the software will produce a map such as seen in figure 5.5 a).

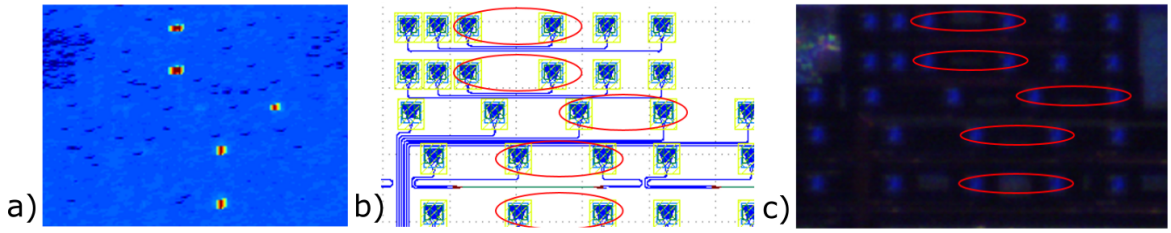

Figure 5.5: a) The result of the MapGC, with red indicating a signal in this position. b) Design schematic of this region with the corresponding GC pairs circled. c) View on the camera.

Snap to GC and Fine Align

Once the map is done, the user can move the fiber to anywhere on the map by clicking Snap to GC, positioning the cross-hair over the red spot and clicking again.

In order to get good transmission, a Fine Align must be run. This function optimizes the X and Y down to micrometer accuracy.

The device is then in position to be tested optimally.

Wavelength sweep

Often, the most informative data set to acquire is the wavelength-dependent response of a device, represented as the transmission on a logarithmic scale versus the wavelength. This data enables us to evaluate the loss in the device, the performance of a filter, the resonance of a cavity or the behavior of an interferometer.

A function to measure this response is available directly in the laser and detector mainframe and accessible via the Manual Coordinates Control Window. The settings include the minimal and maximal wavelength, the resolution and the number of sweeps for averaging. When multiple detectors are available, check only the ones that are needed.

During the sweep, the laser is tuned at each wavelength in quick succession, while the detector measures the incoming power. The output is a plot of the power versus the wavelength.

Automated measurement

The Matlab script can perform automated measurement of many devices without human input, as long as switching from one device to an other only requires to move the X and Y coordinates.

To do so, the software requires a list of all the devices with their coordinates (see section 5.3.4), as well as 3 points not on the same straight line in order to find the exact correspondence between the stage coordinates and the design coordinates.

To input a point, align with a device, select this device's name from the list in the Coordinates frame under GDS device and press Set. The stage and design coordinates for this point will be saved.

After 3 points, the software will calculate the coordinate transformation, and will unlock the Devices and Test tabs.

In the Devices tab, check all the devices that need to be tested, then proceed to the Test tab and press Start. The stage will move by itself to each device one by one, doing the alignment and sweep the same way they have been setup previously. The results are previewed as the measurements take place and a green or red color indicates if a signal was measured for each device. The results are saved in multiple formats to the folder provided in the Task tab.

5.3.2 Alignment devices

A fundamental device that should be included on all chips is the alignment mark. It consist of a pair of optical input and output connected to each other with a standard waveguide and few bends. It is the most simple device possible, and serves multiple purposes.

First, since all other devices are usually measured through an optical input and output, alignment marks allow you to calculate the response of the device alone, by subtracting the response of the FGCs. When doing this subtraction (in dB), be aware that the response of FGC sometimes has a lot of variation across the chip and that the average of marks close to the device will give the most accurate result.

Second, since there might be unforeseen issues or loss, one cannot always expect to get a

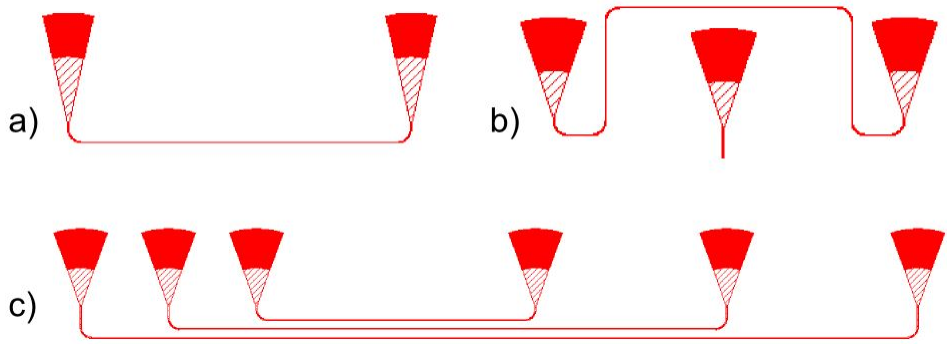

Figure 5.6: a) A simple alignment mark. b) An alignment mark use to better locate an other FGC. c)Alignment marks for multiple pitches between fibers.

transmission into an unknown device. Since alignment marks are the most simple device, they have the lowest chance of failure and should be the first thing you align with when starting a test session. Otherwise, it can be difficult to asses whether the alignment is good or not if there is no transmission.

When using different types of FGCs, create alignment marks for each type.

5.3.3 Low SSE

The laser sources used in the lab (Agilent HP 81680A) are actually two lasers in one. The first mode is a high power laser. The other, called Low SSE, which stands for low Spontaneous Source Emission, has a lower power, but has a better sidelobes suppression.

While the lasers have the majority of their power in a very narrow line-width, other wavelengths are also emitted spontaneously or in suppressed side modes. The typical extinction ratio is over 40 dB, but if more precision is required, the Low SSE mode can be used and go up to 60 dB of contrast.

The normal laser and the Low SSE one do no have the same output port on the laser, so the fiber must be switched when changing mode. In the software, there is a LowSSE option in the settings menu of all functions, which needs to be in the right mode. To verify that you are connected and using the right laser, check the Active LED indicator on the laser itself, as both lasers have separate indicators.

5.3.4 Names labels and coordinate files

In order to create the coordinate file used by the automated measurement script, one must label the position and name of each device on the design (GDS file). A text object must be created on the tip of each optical input. The coordinates and text of this object are what is used to create the file.

To create a coordinate file from a GDS with labels, one can use a custom KLayout script called "Create coordinate file" under the Tools menu. This script is installed on the laboratory workstations.

When naming devices, it is customary to use the prefix "opt_in" to differentiate optical inputs labels from other labels. The next part of the name should start with a letter and be a unique identifier. Indicate the operating wavelength and polarization of the device for reference at measurement.

5.3.5 Electrical Probes

It is often required to measure the optical properties of a system with different kinds of electrical inputs.

Do the optical alignment first. Touch very lightly with the electrical probe to keep the chip aligned. Verify there is a good contact with a low voltage and check for current.

When your input is a radio frequency (RF) signal, you need a contact before applying the signal. Otherwise, reflections can damage the equipment if there is no contact. Thus, verify the contact with direct current (DC) input first.

If possible, use a station where the optical fiber array moves instead of the chip stage to be able to realign the optical input once electrically probed. Fix the chip in place with adhesive or suction if possible.

Refer to equipment manuals and specialists, especially for RF measurements. RF equipments are both fragile and expensive and should always be used with the proper precautions. Make sure you use the right connector type and wear anti-static footwear and wrist-band.

5.4 Phase Measurements with OVA

All of the phase measurements in this memoir were measured with the Luna OVA. While the tunable laser and detector combination allows to measure the amplitude response of the filter, it provides no information on the phase. To get the phase measurement, one must use coherent detection, which is usually done by interfering the output of the system with its input.

This measurement is performed with an optical vector analyzer (OVA), a commercial device available in our laboratories and manufactured by Luna. This device has two optical ports: one laser output/reflection input and one transmission input. It can be used both to measure the response of transmissive and reflective filters. It has an internal laser and thus can be used by simply connecting and calibrating it. Refer to the manufacturer's instructions for calibration.

The Luna OVA is operated with the accompanying computer station and the OVA software. Once calibrated, input all the relevant parameters such as wavelength range and proceed with the measurement. The instrument will measure the Jones matrix of the system, which is the full linear response of the device under test for each polarization. From this measurement, the software can calculate the insertion loss, the group delay and the chromatic dispersion, among other things.

It is suggested to save the data in binary (.bin) format. While this format is not readily readable, Nicolas Ayotte developed a Matlab code to interpret it, *LunaBinary.m* which allows the user to access all the calculations available in the OVA software.

Conclusion

This concludes my memoir about contra-directional couplers on the silicon on insulator platform, which still offer a lot of unanswered research topics. A critical performance metric to work upon in most systems is optical loss, and future work could try to reduce it by using other materials with lower absorption, such as silicon nitride.

This research focused on relatively wide bandwidths, but many applications, such as dense WDM, require filters with bandwidths in the 10 to 100 GHz range. Thus, it would be interesting to investigate the lower limits of contra-DC filters, perhaps using the inverse layer peeling algorithm.

System level considerations were not discussed in detail, and while system designers often provide targets to achieve for figures of merit such as dispersion, it would be interesting to have a clearer picture of the role of filters in applications and where contra-directional couplers can be advantageously used.

While the filter presented in chapter 4 has a tunable drop port, the through port cannot be tuned to smaller bandwidth and a part of the signal is potentially lost. Completely reconfigurable networks will require both drop and through port tunability, which might be achieved in some way by reconnecting the tapered ports.

The present implementation of contra-DCs only work for a single polarization. The fiber input polarization is often random and the usual solution to this issue is to use polarization diversity, i.e. split the TE and TM components in separate identical circuits. While optical birefringence is inherent to any cross-section with directionality, such as a pair of waveguides, it might be possible to compensate the birefringence and create a polarization insensitive contra-directional coupler.

To answer some of these challenges, one tool that has not been looked into thoroughly for contra-DCs is subwavelength gratings, or meta-materials. By using patterning features much smaller than the wavelength, it is possible to create regions optically analogous to low index materials. Such structures resulted in more optimal performances for other silicon photonics devices, and it remains to be seen if it could also bring improvements to contra-DCs.

Bibliography

[1] Matrix exponential - matlab expm.

[2] B Ben Bakir, A Vazquez de Gyves, R Orobtchouk, P Lyan, C Porzier, A Roman, and JM Fedeli. Low-loss ($<$ 1 db) and polarization-insensitive edge fiber couplers fabricated on 200-mm silicon-on-insulator wafers. IEEE Photon. Technol. Lett, 22(11):739–741, 2010.

[3] Michael Caverley, Nicolas AF Jaeger, and Lukas Chrostowski. Measurement of optical losses in silicon photonic contra-directional couplers. In Photonics North, 2015, pages 1–1. IEEE, 2015.

[4] Yunhong Ding, Minhao Pu, Liu Liu, Jing Xu, Christophe Peucheret, Xinliang Zhang, Dexiu Huang, and Haiyan Ou. Bandwidth and wavelength-tunable optical bandpass filter based on silicon microring-mzi structure. Optics express, 19(7):6462–6470, 2011.

[5] Po Dong, Wei Qian, Hong Liang, Roshanak Shafiiha, Dazeng Feng, Guoliang Li, John E Cunningham, Ashok V Krishnamoorthy, and Mehdi Asghari. Thermally tunable silicon racetrack resonators with ultralow tuning power. Optics express, 18(19):20298–20304, 2010.

[6] Raphaël Dubé-Demers, Jonathan St-Yves, Antoine Bois, Qiuhang Zhong, Michael Caverley, Yun Wang, Lukas Chrostowski, Sophie LaRochelle, David V Plant, and Wei Shi. Analytical modeling for ultra-high-speed microring modulators with electrical and optical dynamics. In Optical Communication (ECOC), 2014 European Conference on, pages 1–3. IEEE, 2014.

[7] Bradley J Frey, Douglas B Leviton, and Timothy J Madison. Temperature-dependent refractive index of silicon and germanium, 2006.

[8] David J Geisler, Nicolas K Fontaine, Ryan P Scott, and SJB Yoo. Demonstration of a flexible bandwidth optical transmitter/receiver system scalable to terahertz bandwidths. Photonics Journal, IEEE, 3(6):1013–1022, 2011.

[9] William M Green, Michael J Rooks, Lidija Sekaric, and Yurii A Vlasov. Ultra-compact, low rf power, 10 gb/s silicon mach-zehnder modulator. Optics express, 15(25):17106–17113, 2007.

[10] Gerhard Heinzel, Albrecht Rüdiger, and Roland Schilling. Spectrum and spectral density estimation by the discrete fourier transform (dft), including a comprehensive list of window functions and some new at-top windows. 2002.

[11] Folkert Horst, William MJ Green, Solomon Assefa, Steven M Shank, Yurii A Vlasov, and Bert Jan Offrein. Cascaded mach-zehnder wavelength filters in silicon photonics for low loss and flat pass-band wdm (de-) multiplexing. Optics express, 21(10):11652–11658, 2013.

[12] Folkert Horst, William MJ Green, Solomon Assefa, Steven M Shank, Yurii A Vlasov, and Bert Jan Offrein. Cascaded mach-zehnder wavelength filters in silicon photonics for low loss and flat pass-band wdm (de-) multiplexing. Optics express, 21(10):11652–11658, 2013.

[13] Masahiko Jinno, Hidehiko Takara, Bartlomiej Kozicki, Yukio Tsukishima, Yoshiaki Sone, and Shinji Matsuoka. Spectrum-efficient and scalable elastic optical path network: architecture, benefits, and enabling technologies. Communications Magazine, IEEE, 47(11):66–73, 2009.

[14] Raman Kashyap. Fiber bragg gratings. Academic press, 1999.

[15] Guoliang Li, Ashok V Krishnamoorthy, Ivan Shubin, Jin Yao, Ying Luo, Hiren Thacker, Xuezhe Zheng, Kannan Raj, and John E Cunningham. Ring resonator modulators in silicon for interchip photonic links. Selected Topics in Quantum Electronics, IEEE Journal of, 19(6):95–113, 2013.

[16] Ansheng Liu, Ling Liao, Doron Rubin, Hat Nguyen, Berkehan Ciftcioglu, Yoel Chetrit, Nahum Izhaky, and Mario Paniccia. High-speed optical modulation based on carrier depletion in a silicon waveguide. Optics Express, 15(2):660–668, 2007.

[17] Katsunari Okamoto. Wavelength-division-multiplexing devices in thin soi: advances and prospects. Selected Topics in Quantum Electronics, IEEE Journal of, 20(4):248–257, 2014.

[18] Katsunari Okamoto and Kenzo Ishida. Fabrication of silicon reflection-type arrayed-waveguide gratings with distributed bragg reflectors. Optics letters, 38(18):3530–3533, 2013.

[19] Jun Rong Ong, Ranjeet Kumar, and Shayan Mookherjea. Ultra-high-contrast and tunable-bandwidth filter using cascaded high-order silicon microring filters. Photonics Technology Letters, IEEE, 25(16):1543–1546, 2013.

[20] Piero Orlandi, Carlo Ferrari, Michael John Strain, Antonio Canciamilla, Francesco Morichetti, Marc Sorel, Paolo Bassi, and Andrea Melloni. Reconfigurable silicon filter with continuous bandwidth tunability. Optics letters, 37(17):3669–3671, 2012.

[21] Wei Shi, Wang, Charlie Lin, Han Yun, Yang Liu, Tom Baehr-Jones, Michael Hochberg, Nicolas AF Jaeger, and Lukas Chrostowski. Silicon photonic grating-assisted, contra-directional couplers. Optics express, 21(3):3633–3650, 2013.

[22] Wei Shi, Han Yun, Charlie Lin, Jonas Flueckiger, Nicolas AF Jaeger, and Lukas Chrostowski. Coupler-apodized bragg-grating add–drop filter. Optics letters, 38(16):3068–3070, 2013.

[23] Wei Shi, Han Yun, Charlie Lin, Mark Greenberg, Xu Wang, Yun Wang, Sahba Talebi Fard, Jonas Flueckiger, Nicolas AF Jaeger, and Lukas Chrostowski. Ultra-compact, flat-top demultiplexer using anti-reflection contra-directional couplers for cwdm networks on silicon. Optics express, 21(6):6733–6738, 2013.

[24] Wei Shi, Han Yun, Charlie Lin, Xu Wang, Jonas Flueckiger, Nicolas Jaeger, and Lukas Chrostowski. Silicon cwdm demultiplexers using contra-directional couplers. In CLEO: Science and Innovations, pages CTu3F–5. Optical Society of America, 2013.

[25] Alexandre D Simard, Nicolas Ayotte, Yves Painchaud, S Bedard, and S LaRochelle. Impact of sidewall roughness on integrated bragg gratings. Journal of Lightwave Technology, 29(24):3693–3704, 2011.

[26] Alexandre D Simard, Guillaume Beaudin, Vincent Aimez, Yves Painchaud, and Sophie LaRochelle. Characterization and reduction of spectral distortions in silicon-on-insulator integrated bragg gratings. Optics express, 21(20):23145–23159, 2013.

[27] Alexandre D Simard, Nezih Belhadj, Yves Painchaud, and Sophie LaRochelle. Apodized silicon-on-insulator bragg gratings. Photonics Technology Letters, IEEE, 24(12):1033–1035, 2012.

[28] Alexandre D. Simard and Sophie LaRochelle. High-quality bragg gratings operating in reflection without circulators in soi. In CLEO: 2015, page SM3I.6. Optical Society of America, 2015.

[29] Alexandre D Simard, Yves Painchaud, and Sophie LaRochelle. Integrated bragg gratings in spiral waveguides. Optics express, 21(7):8953–8963, 2013.

[30] Johannes Skaar, Ligang Wang, and Turan Erdogan. On the synthesis of fiber bragg gratings by layer peeling. Quantum Electronics, IEEE Journal of, 37(2):165–173, 2001.

[31] Wojciech Śmigaj, Javier Romero-Vivas, Boris Gralak, Liubov Magdenko, Béatrice Dagens, and Mathias Vanwolleghem. Magneto-optical circulator designed for operation in a uniform external magnetic field. Optics letters, 35(4):568–570, 2010.

[32] Jonathan St-Yves, Hadi Bahrami, Philippe Jean, Sophie LaRochelle, and Wei Shi. Widely bandwidth-tunable silicon filter with an unlimited free-spectral range. Opt. Lett., 40(23):5471–5474, Dec 2015.

[33] Jonathan St-Yves, Sophie LaRochelle, and Wei Shi. O-band silicon photonic bragg-grating multiplexers using uv lithography. In Optical Fiber Communication Conference, pages Tu2F–7. Optical Society of America, 2016.

[34] GV Treyz, Paul G May, and Jean-Marc Halbout. Silicon optical modulators at 1.3-mu m based on free-carrier absorption. Electron Device Letters, IEEE, 12(6):276–278, 1991.

[35] Diedrik Vermeulen, S Selvaraja, Pl Verheyen, G Lepage, W Bogaerts, P Absil, D Van Thourhout, and G Roelkens. High-efficiency fiber-to-chip grating couplers realized using an advanced cmos-compatible silicon-on-insulator platform. Optics express, 18(17):18278–18283, 2010.

[36] Jinsong Xia, Jinzhong Yu, Zhangtao Wang, Zhongchao Fan, and Shaowu Chen. Low power 2× 2 thermo-optic soi waveguide switch fabricated by anisotropy chemical etching. Optics communications, 232(1):223–228, 2004.

[37] Qianfan Xu, Sasikanth Manipatruni, Brad Schmidt, Jagat Shakya, and Michal Lipson. 12.5 gbit/s carrier-injection-based silicon micro-ring silicon modulators. Optics express, 15(2):430–436, 2007.

[38] Qianfan Xu, Brad Schmidt, Jagat Shakya, and Michal Lipson. Cascaded silicon micro-ring modulators for wdm optical interconnection. Optics express, 14(20):9431–9435, 2006.

[39] Han Yun, Wei Shi, Yun Wang, Lukas Chrostowski, and Nicolas AF Jaeger. 2× 2 adiabatic 3-db coupler on silicon-on-insulator rib waveguides. In Photonics North 2013, pages 89150V–89150V. International Society for Optics and Photonics, 2013.

[40] Bo Zhang, David Leuenberger, Ming-Chang M. Lee, A.E. Willner, and M.C. Wu. Experimental demonstration of dynamic bandwidth allocation using a mems-actuated bandwidth-tunable microdisk resonator filter. Photonics Technology Letters, IEEE, 19(19):1508–1510, Oct 2007.

[41] Yi Zhang, Shuyu Yang, Andy Eu-Jin Lim, Guo-Qiang Lo, Christophe Galland, Tom Baehr-Jones, and Michael Hochberg. A compact and low loss y-junction for submicron silicon waveguide. Optics express, 21(1):1310–1316, 2013.

[42] Qiuhang Zhong, Venkat Veerasubramanian, Yun Wang, Wei Shi, David Patel, Samir Ghosh, Alireza Samani, Lukas Chrostowski, Richard Bojko, and David V Plant. Focusing-curved subwavelength grating couplers for ultra-broadband silicon photonics optical interfaces. Optics express, 22(15):18224–18231, 2014.